materials

MDPI

Review

Carbon-Based Composites for Oxygen Evolution Reaction Electrocatalysts: Design, Fabrication, and Application

Chang Gao, Haiyu Yao, Peijie Wang, Min Zhu, Xue-Rong Shi * and Shusheng Xu *

School of Material Science and Engineering, Shanghai University of Engineering Science, Shanghai 201620, China
* Correspondence: shixuer05@mails.ucas.ac.cn (X.-R.S.); xushusheng@sues.edu.cn (S.X.)

Abstract: The four-electron oxidation process of the oxygen evolution reaction (OER) highly influences the performance of many green energy storage and conversion devices due to its sluggish kinetics. The fabrication of cost-effective OER electrocatalysts via a facile and green method is, hence, highly desirable. This review summarizes and discusses the recent progress in creating carbon-based materials for alkaline OER. The contents mainly focus on the design, fabrication, and application of carbon-based materials for alkaline OER, including metal-free carbon materials, carbon-based supported composites, and carbon-based material core–shell hybrids. The work presents references and suggestions for the rational design of highly efficient carbon-based OER materials.

Keywords: carbon-based materials; oxygen evolution reaction; metal-free; support; core–shell; rational design

check for updates

Citation: Gao, C.; Yao, H.; Wang, P.; Zhu, M.; Shi, X.-R.; Xu, S. Carbon-Based Composites for Oxygen Evolution Reaction Electrocatalysts: Design, Fabrication, and Application. *Materials* **2024**, *17*, 2265. https://doi.org/10.3390/ma17102265

Academic Editors: Dariusz Szpica, Andrzej Borawski and Grzegorz Mieczkowski

Received: 1 April 2024
Revised: 30 April 2024
Accepted: 7 May 2024
Published: 11 May 2024

Copyright: © 2024 by the authors. Licensee MDPI, Basel, Switzerland. This article is an open access article distributed under the terms and conditions of the Creative Commons Attribution (CC BY) license (https://creativecommons.org/licenses/by/4.0/).

1. Introduction

In order to deal with the issues caused by the fossil fuel energy system, such as energy security and climate change, the development of sustainable clean energy is imperative. Hydrogen is regarded as an ideal secondary energy carrier due to its high energy density. Hydrogen production by electrolysis uses green electricity in the form of solar and wind energy and plays a crucial role in the storage, transformation, and efficient utilization of clean energy [1–3]. However, improving the efficiency of hydrogen production and controlling the cost of hydrogen production have been bottlenecks that have restricted the large-scale application of related technologies.

Techniques for hydrogen production through the electrolysis of water include alkaline water electrolysis (AWE [4–6]), proton exchange membrane water electrolysis (PEMWE) [7,8], anion exchange membrane water electrolysis (AEMWE) [9], and high-temperature solid oxide water electrolysis (SOWE) [10]. Among them, AWE has been successfully commercialized. However, AWE still faces several problems, such as environmental pollution, equipment corrosion, and low hydrogen production efficiency (59~70%). The oxygen evolution reaction (OER), a half-reaction of hydrogen production by water electrolysis, involves four-electron reaction kinetics. Generally, the OER follows the adsorbate evolution mechanism (AEM). The reaction occurs in alkaline solutions according to Equations (1)–(4):

$$* + OH^- \rightarrow OH^* + e^- \quad (1)$$

$$OH^* + OH^- \rightarrow O^* + H_2O + e^- \quad (2)$$

$$O^* + OH^- \rightarrow OOH^* + e^- \quad (3)$$

$$OOH^* + OH^- \rightarrow * + O_2 + H_2O + e^- \quad (4)$$

The * means the free surface site. The thermodynamic limiting potential U_L is calculated by Equation (5):

$$U_L = \max\{\Delta G_1, \Delta G_2, \Delta G_3, \Delta G_4\}/e \quad (5)$$

However, thermodynamic constraints on the scaling relationship between the Gibbs free energies of *OOH and *OH result in a minimum theoretical overpotential of 370 mV for the optimal catalyst [11]. For oxides-based electrocatalysts, an OER mechanism based on oxygen redox chemistry, namely, the lattice oxygen oxidation mechanism (LOM) [12], has been reported recently. The LOM pathway includes five steps [13]:

$$*O_l\ H + OH^- \rightarrow *O_l + H_2O + e^- \quad (6)$$

$$*O_l + OH^- \rightarrow *O_l\ OH + e^- \quad (7)$$

$$*O_l\ OH + OH^- \rightarrow *O_l\ O + H_2O + e^- \quad (8)$$

$$*O_l\ O \rightarrow O_{vacancy}* + O_2 \quad (9)$$

$$O_{vacancy}* + OH^- \rightarrow *OH + e^- \quad (10)$$

where O_l and $O_{vacancy}$* denote the lattice oxygen atoms and lattice oxygen vacancy site, respectively. LOM can bypass O-O bond formation and break the limit of the proportional relationship.

OER is the bottleneck of hydrogen production by water electrolysis [14]. OER also plays a vital role in the performance of other clean energy conversion and storage devices, such as metal–air batteries and CO_2 reduction [15,16]. The present OER electrocatalysts are mostly the precious metal oxides IrO_2 and RuO_2, limiting their large-scale application. In order to improve hydrogen production efficiency and reduce production costs, active and low-cost OER electrocatalysts have been developed. To date, nonprecious metal oxides, phosphides, sulfides, and alloys have been reported as efficient OER electrocatalysts [17,18]. The OER process of some perovskite electrocatalysts and NiFe-based (oxy)hydroxide follows the LOM mechanism [12]. For RuO_2, the lattice oxygen is not involved in OER [12]. A comprehensive understanding of the oxygen redox in LOM and possible characterization techniques that can be used to identify the oxygen redox are reviewed in Ref. [19]. After years of effort, significant progress has been made in the design, preparation, and application of high-performance OER materials, including carbon-based materials (Figure 1) [20–23]. Efficient nonprecious metal oxides, phosphides, sulfides, and alloys can typically reach a current density of 10 mA cm^{-2} at an overpotential <300 mV in 1.0 M KOH [20–23].

In 2011, Liang et al. [24] fabricated carbon-based materials for effective OER electrocatalysts. They reported a hybrid material consisting of Co_3O_4 nanocrystals grown on reduced graphene oxide (rGO) to be an efficient bi-functional catalyst for the oxygen reduction reaction (ORR) and OER. Although Co_3O_4 or rGO alone show poor catalytic activity, their hybrid is highly active for OER. The N doping of rGO further boosts OER performance [24]. Inspired by these results, researchers have performed many relevant works and made significant progress [25]. Common electrocatalysts for carbon-based OER materials include metal-free carbon or polymer-based materials, such as covalent organic frameworks (COFs) [26], porous organic polymers (POPs) [27], and composites of carbon and nonprecious metal-containing composite, such as CoP/carbon-cloth (CC), MCoP/CC [28], O-Co-N/C [29], and others [30].

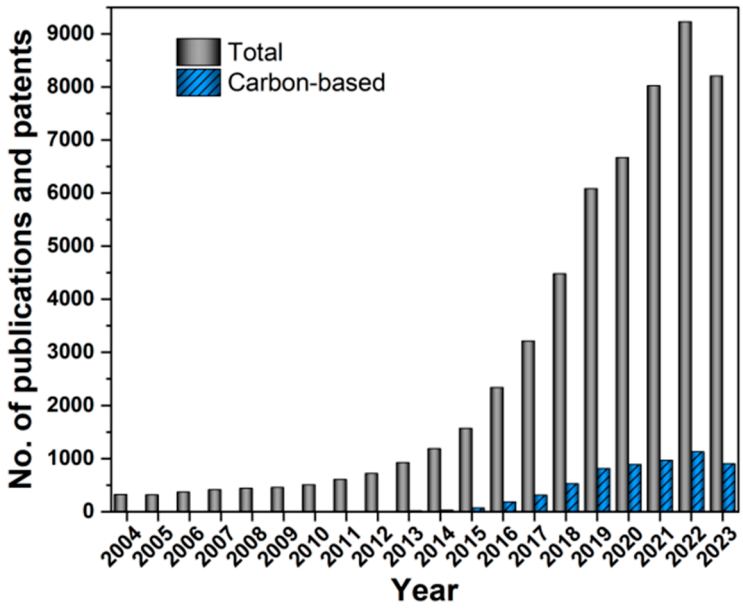


Figure 1. Papers and patents published over the past 20 years that cover oxygen evolution reaction, water splitting, and carbon. Data from the Web of Science.

The following review summarizes the research progress and achievable performance levels of carbon-based composites for OER. It aims to provide references and guidance for developing nonprecious metal anode materials for the alkaline electrolysis of water. If the electrocatalyst can work at high current density (HCD), the performance of the electrocatalyst at HCD will be discussed in a separate subsection.

2. Design of Carbon-Based Composites

2.1. Theoretical Design

With the development of computational methods, especially the in-depth integration of big data and artificial intelligence, various computational methods have been employed to reduce the cost of catalyst development. Computational methods such as density-functional theory (DFT), molecular dynamics, and machine learning (ML) are widely employed for catalyst pre-screening. On this basis, materials are synthesized for verification to realize the rational design of high-efficiency OER electrocatalysts [31–35]. On the other hand, due to the complex four-electron reaction mechanism involved in OER, one of the current research goals is to find simple structural descriptors (such as the electronegativity or the radius of an element) to reveal the structure–activity relationship instead of fully investigating the reaction mechanism to achieve rational design and rapid pre-screening.

Based on the AEM mechanism, Li's group [36] used a combination of topology-based ML and first-principles calculations to select 511 carbon surface-supported transition metal double-atom catalysts (DACs) out of 16,767 structures with catalytic performance outperforming IrO_2(110) (Figure 2a,b) for OER. The fitting accuracy of the model for OER activity on the test set was 0.957 (Figure 2c), indicating that the machine learning model can accurately predict the OER catalytic activity of carbon-supported DACs. Figure 2d shows the predicted OER activity results for all DACs. The results showed that carbon surface-supported transition metal double-atom electrocatalysts containing Ni, Cu, Zn, Pd, Ag, Cd, Pt, and Au elements exhibited the best OER catalytic activity [36]. Although DACs containing Au, Zn, and Cd elements can be stably fixed on the defects of a carbon substrate, they have relatively lower stability than other double-atom OER electrocatalysts [36]. Using ML and DFT, Fang et al. [37] screened hundreds of potential dual-metal-site electrocatalysts (DMSCs) and found 10 DMSCs with OER activity superior to RuO_2. Similarly, Yao et al. [38] performed DFT and ML predictions to systematically investigate the bifunctional OER/ORR activity of 3d transition metal (TM) atom-doped g-C_3N_3. ML predictions

identified the 3d band center (εd) as the most effective descriptor of the overpotential of OER. Ye et al. [39] employed high-throughput calculations to successfully screen catalytic structures comparable to IrO_2(110) for OER from a total of 78 edge-anchored single-atom electrocatalysts (E-SACs) based on 26 TM species with three coordination patterns. E-Rh-N_4-C, in particular, is expected to be an efficiently bifunctional electrocatalyst for OER.

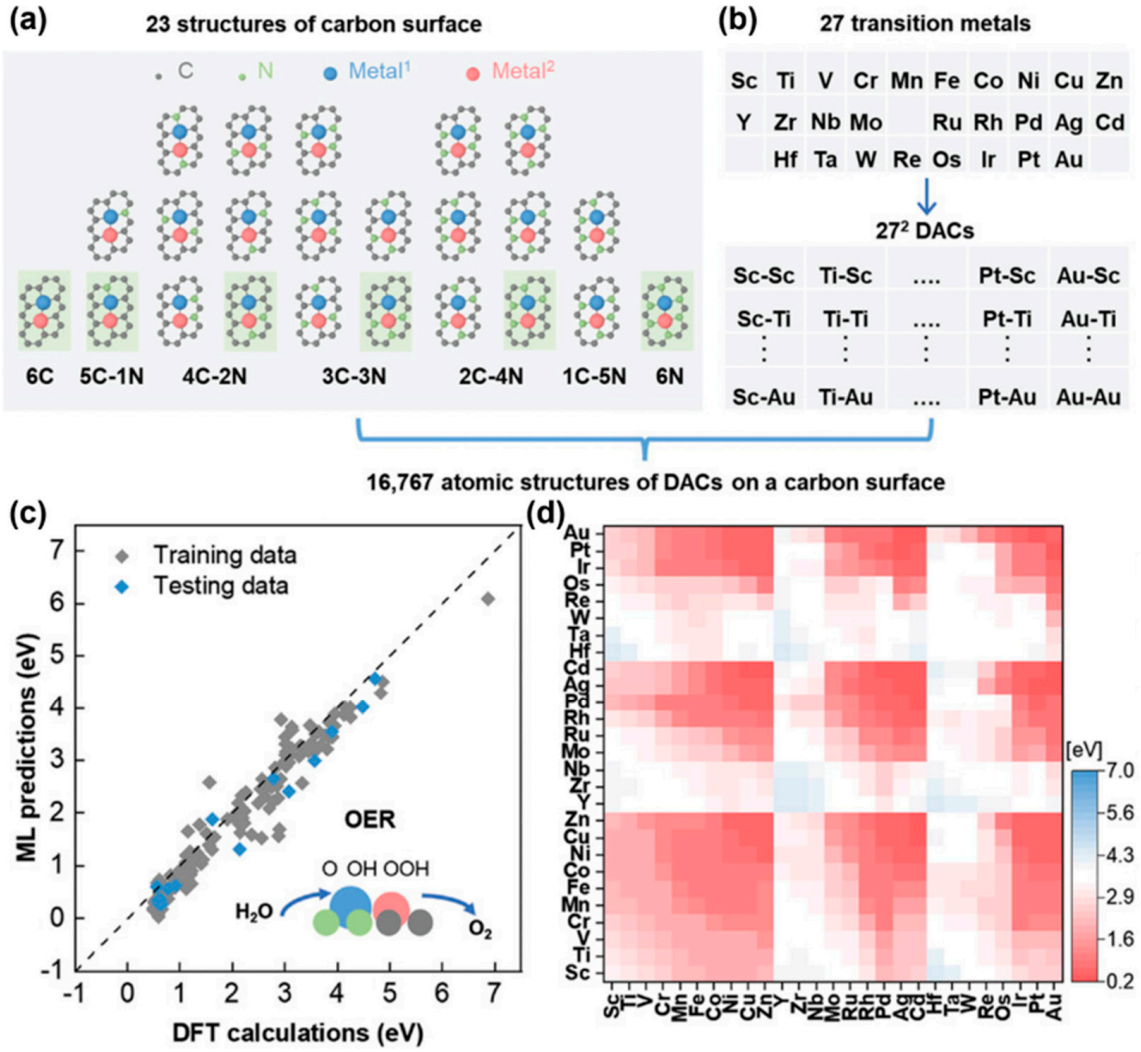


Figure 2. (**a**) A total of 23 types of carbon surface defect structures categorized into seven groups by their N doping level. (**b**) A total of 729 (27 × 27) possible compositional combinations of double-atom electrocatalysts lead to a total of 16,767 (729 by 23) atomic structures on a carbon surface. (**c**) DFT-calculated OER overpotentials versus predictions from the ML model on the training and testing subsets. (**d**) ML-predicted OER overpotentials of all DACs on a symmetric defect structure [36].

2.2. Combined Theoretical and Experimental Design

The joint strategy of computational prediction–experimental verification–computational interpretation is also widely employed. This method can conduct systematic research on a certain catalyst system, achieving mutual verification between calculations and experiments, but it usually requires considerable work. Zhang et al. [40] designed and developed a series of CC self-supported bimetallic phosphides for high-performance OER. Their DFT calculations revealed that Fe/Ni/Mn doping can regulate the electronic properties of CoP, thereby affecting its adsorption ability for key species. On this basis, a series of binder-free MCoP/CC (M = Fe, Ni, or Mn) was synthesized via a hydrothermal–phosphating method. The resulting MCoP/CC achieved high-performance OER in alkaline and simulated seawater solutions with overpotentials at 10 mA cm^{-2} η_{10} lower than 299 mV. A similar com-

bined theory–experiment method has been employed by other groups [41]. For example, Jia et al. [41], Zhang et al. [42], and Li et al. [43] all found that defects played a crucial role in the individual electrocatalytic activity for alkaline OER experimentally and theoretically.

2.3. Experimental Design

Various experimental methods have been adopted to improve the activity and stability of OER electrocatalysts. Commonly used strategies include defect engineering, such as heteroatom doping or vacancy introduction [44]; structural control, such as the regulation of morphology and electronic structure [28,45–48]; and interface engineering [42], such as constructing composites [49,50]. Studies have confirmed that carbon–metal composites can effectively adjust the catalyst's electronic properties, avoid the metal's dissolution in the electrolyte, and consequently improve electrocatalysts' intrinsic activity and stability [51–55]. Regarding the regulation of structural morphology, researchers are committed to the design of hierarchical structures. In particular, nanoarrays, nanospheres, and nanoflowers assembled from one-dimensional nanowires and two-dimensional (2D) nanosheets exhibit excellent OER performance. This is because such hierarchical structures typically have a large specific surface area, exposing abundant reaction sites and sufficient interface sites that provide channels for rapid electron transfer.

3. Fabrication and Application

At present, the commonly used preparation method for metal-free COFs and POPs is the solvothermal/hydrothermal strategy [27]. To obtain the conductive carbon support/shell, scientists have widely employed Prussian blue analogs (PBAs) [56–58], metal–organic frameworks (MOFs) [59,60], and biomass-derived carbon sources, e.g., chitosan [61], as the carbon matrix precursor due to their adjustable porous structure and a variety of heteroatomic functional groups [62–67]. Using heteroatoms with more electrons than C, such as S, N, and P, not only improves conductivity but also induces point defects, promoting OER [68]. In this case, the formation of the (heteroatom-doped) carbon layer is usually through high-temperature calcination. Another simple way of fabricating carbon-based composites is to add carbon-based materials directly during the preparation process, such as CC or carbon nanotubes (CNTs) [69].

In the following sections, we first discuss metal-free carbon-based OER materials. The content of carbon-based composites for OER is organized based on the architecture created by the combined carbon-supported and core–shell architecture.

3.1. Metal-Free Carbon-Based Materials

After years of investigation, metal-free COFs and POPs-based materials with comparable activity to IrO_2/RuO_2 have been found. Ghosh et al. strategically designed a noble metal-free thiadiazole (TDA) and triazine (Trz) linked porous organic polymer (TDA-Trz-POP) having a N- and S-rich surface [27]. This scrunch paper type TDA-Trz-POP has an η_{10} value of 410 mV and a lower Tafel slope of 104.5 mV deg^{-1} for OER in 1.0 M KOH. Another series of thianthrene-based sp^2 C = C bonded POPs (Figure 3a) with hollow spherical morphologies (Figure 3b,c), synthesized by Sadhukhan et al. [70], exhibit a superior OER activity. The most efficient bifunctional (hydrogen evolution reaction HER and OER) electrocatalyst THT-PyDAN (Figure 3a) was screened out based on structural tuning to explore the effects of heteroatom incorporation, hydrophilicity, and variations in linker length on electrocatalytic activity. It delivers an η_{10} value of 283 mV in 1.0 M KOH for OER (Table 1, Figure 3d), surpassing all previously reported metal-free bifunctional electrocatalysts. Moreover, THT-PyDAN performs even after 1000 cyclic voltammetry (CV) cycles. A mechanism study by post-catalytic characterization and DFT calculations demonstrated that the intermediates in OER determine the most favorable adsorption site. O * preferentially binds to the S atom of THT-PyDAN, while OH * and OOH * preferentially adsorb on the C atom of the CN group. The potential rate-limiting step is the third step, $O^* + OH^- \rightarrow OOH^* + e^-$ [70]. To overcome the chemical stability issue of metal-free POPs-

based structures, a unique strategy is reported [71] by designing robust imidazole-linked POPs via tandem reversible/irreversible bond formation.

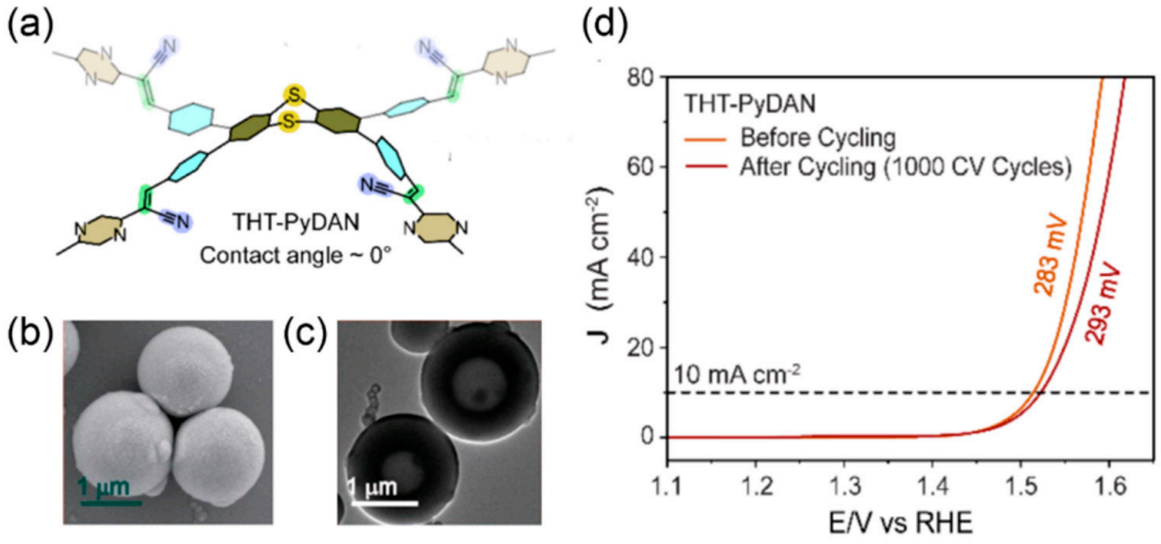


Figure 3. (**a**) Molecular structure, (**b**) SEM image, (**c**) TEM image of THT-PyDAN, and (**d**) its alkaline OER performance before and after 1000 CV cycles [70].

In addition to COPs and POPs, other metal-free carbon-based materials with a 2D structure, such as graphitic carbon nitride (g-C_3N_4), graphene, and reduced graphene oxide (rGO) are also potential OER electrocatalysts [72]. Among them, biomass-derived carbon materials stand out due to their outstanding features, such as ecological friendliness, abundance, free availability, renewability, high specific surface area, ideal conductivity, controllable porosity, and excellent thermal/chemical stability [73]. Many biomass materials have been used as a carbon source, such as chitin [74], *Platycladus orientalis* tree-cone bio waste [75], and corn stalks [76]. For example, the chitin-derived N-doped carbon material developed by Zhao et al. [74] delivered a comparable alkaline OER performance to iridium and cobalt oxides. Nicotine-containing tobacco [77] and *Euonymus japonicus* leaves [78] were also used as a low-cost raw material to synthesize N-doped ordered mesoporous carbon and micro-layered carbon for OER, respectively. The enzyme-modified matter is carbonized in N_2 before being pyrolyzed with NH_4Cl in N_2, resulting in a 3D N-doped catalyst with a large number of hierarchical pores. The OER activity of optimal N/E-HPC-900 has a lower onset potential, a larger Tafel slope, and better durability than RuO_2 due to its higher degree of graphitization and level of N doping [79]. Keshab Pandey et al. [80] used coffee waste to fabricate porous carbon for HER and OER. When carbonized at 600 °C for 2 h and activated by KOH at 600 °C, the coffee waste exhibited a low OER overpotential (η_{10} = 230 mV).

Table 1. Comparison of metal-free and carbon-based supported materials for OER and water splitting by overpotential (η, mV); current density (j, mA cm^{-2}); Tafel slope (TS, mV dec^{-1}); and stability (Sta., h).

Materials	Morphology	OER			Water Splitting		Electrolyte	Ref.
		η at j	TS	Sta.	U at j	Stab.		
THT-PyDAN [a]	POPs, hollow sphere	283@10	81	36@20	1.85@10	12@10	1 M KOH	[70]
TDA-Trz-POP	N,S-rich microporous organic polymer powder	410@10	104.5	3@10	2.61@10	N.A.	1 M KOH	[27]
CCW-KOH-600	Coffee waste-derived porous carbon, activated by KOH at 600 °C	230@10	140	24@10	N.A	N.A.	6 M KOH	[80]
g-C_3N_4	Layered composition	355@10	46.8	45@10&50&100	N.A.	N.A.	1 M KOH	[81]

Table 1. *Cont.*

Materials	Morphology	OER			Water Splitting		Electrolyte	Ref.
		η at j	TS	Sta.	U at j	Stab.		
FeNi-C_3N_4-P/NF	Interfacial hetero-structure of FeNi phosphide/C_3N_4 grown on NF	235@100	40.4	55@100	N.A.	N.A.	1 M KOH	[82]
$CoFe_{0.05}P$/CC	Nanorods grown on CC	264@10	102	45@10	1.59@10	24@10	1 M KOH	[40]
Se-NiS_2/CC	Se-doped NiS_2 nanosheets grown on CC	343@50	44.3	30@100	N.A.	N.A.	1 M KOH	[83]
W@$Ni(OH)_2$/CC	$Ni(OH)_2$ nanosheets and tungsten nanograins form a heterogeneous structure on CC	290@10	67	15@1.52 V	N.A.	N.A.	1 M KOH	[84]
d-NiFeP/CC	Array structure grown on CC	185@10	24.56	100@10	1.48@10	50@10	1 M KOH	[85]
TiN@NiO-$NiSe_2$/CC	NiO-$NiSe_2$ hetero-structured nanosheets shelling over 1D TiN nanoarrays supported by CC	240@10	29	10@10	1.57@10	50	1 M KOH	[86]
FeCo/Co_2P/Fe_2P@NPC	FeCo/Co_2P/Fe_2P imbedded in N-doped porous carbon	281@10	85	100@10	1.55@10	24@1.58 V	1 M KOH	[87]
$FeCoP_2$@NPPC	Phosphide embedded in a N and P co-doped porous carbon	236@10	83	12@1.5 V	1.6@10	16@10	1 M KOH	[88]
NiV_2P/FeSe/CC	Ni-Fe-V trimetallic phosphorus–selenium composite grown on CC	168@10 282@200	44.3	160@100	1.53@10	N.A.	1 M KOH	[89]
$CuMn_{0.5}Co_2O_4$/CC	Nanoneedles of spinel oxides grown on CC	189@10 327@200	76.2	24@10	N.A.	N.A.	1 M KOH	[90]
Fe-NiOOH/CQDs [a]	In situ activation of Fe-NiOOH nanoclusters on carbon quantum dots	199@10 450@1000	35	80@10	1.5@10	12@500	1 M KOH	[91]

[a]: The anode and cathode use the same electrode in overall water splitting, with the exception of using Pt/C as the anode. N.A.: Not available.

Graphitic carbon nitride, g-C_3N_4, which consists of tertiary amine-linked periodic heptazine units, is also employed as an alkaline OER electrocatalyst. It can be obtained via a facile one-pot method and used for efficient OER without additional post-treatments or co-catalysts. Torres-Pinto et al. [81] assessed the impact of the preparation temperature (450–650 °C) of g-C_3N_4 on water-splitting processes for the first time and explained it by different characterization techniques (Figure 4). The unique crystal structure, surface chemistry, and electronic properties of the material prepared at 550 °C led to remarkable OER efficiency with a η_{10} of 355 mV and a Tafel slope of 46.8 mV dec^{-1}, defeating the benchmark IrO_2. It had reduced structural distortion and terminal functional groups, which resulted in improved OER activity and durability. It was stable for up to 45 h, even when the applied current density was increased to 100 mA cm^{-2} for 15 h [81].

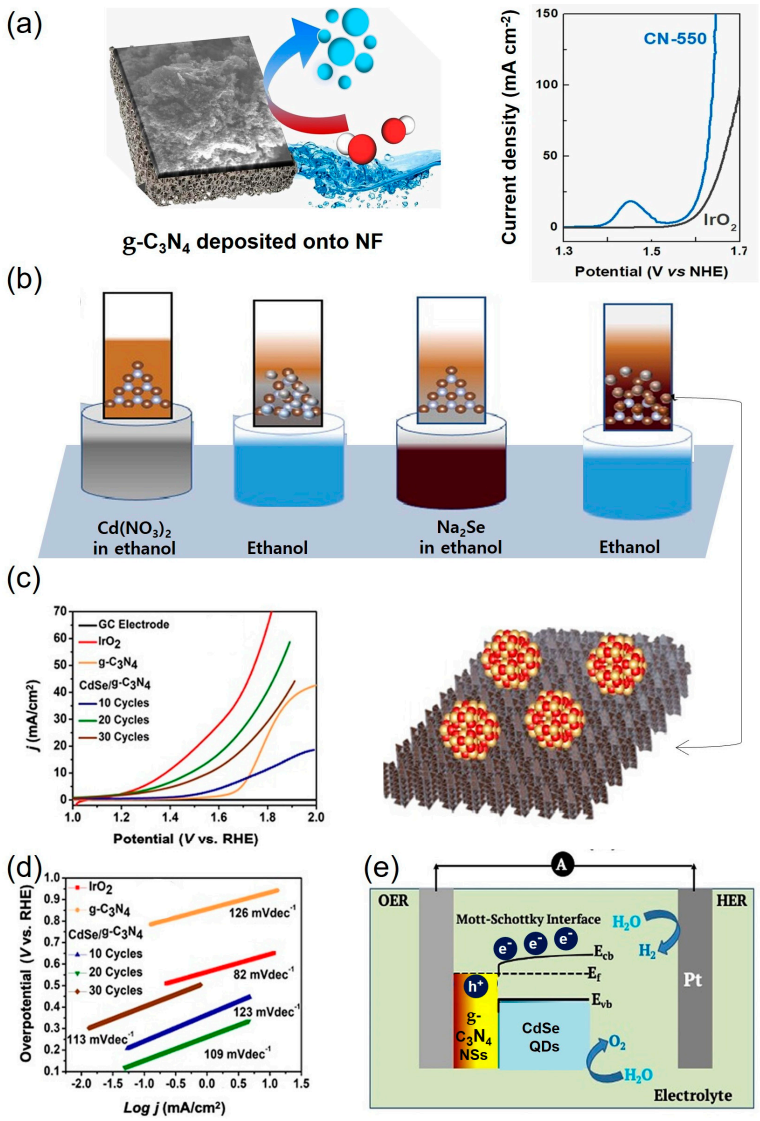


Figure 4. (**a**) The preparation of g-C_3N_4 and linear sweep voltammetry (LSV) polarization curves of alkaline OER [81]. (**b**) Schematic illustration of the synthesis of the CdSe QDs/CN heterostructure through the SILAR method [92] and corresponding (**c**) OER LSV, (**d**) Tafel slopes, and (**e**) charge transfer phenomenon at the interface of the heterostructure in electrocatalysis [92].

Some hybrid materials of biomass-derived carbon and other carbon-based materials, such as CNT and g-C_3N_4, also deliver excellent OER performance. For instance, Wu et al. [93] fabricated chitin-derived N-doped carbon (C-Chitin)/g-C_3N_4 composites via an ultralow-cost route, including the low-temperature dissolution and subsequent carbonization of chitin biomass. The obtained C-Chitin/g-C_3N_4 composites exhibited a well-designed loofa sponge-like three-dimensional (3D) network architecture assembled from many interconnected ultrathin mesoporous nanosheets [93]. Because of the well-designed morphology, a unique mesoporous structure with a high surface density of catalytic active sites, and the combination of N-doped carbon with g-C_3N_4, the C-chitin/g-C_3N_4 composites had high durability in OER [85]. However, metal-free carbon-based materials are not able to reach an industrial current density at a low overpotential.

3.2. Carbon-Based Supported Composites for OER

3.2.1. At Low Current Density (LCD)

Interestingly, in addition to being used as an electrocatalyst directly, g-C_3N_4 can also be used as a substrate of supported OER electrocatalysts, such as oxides, phosphides, and

sulfide-based materials. The nitrogen atoms in g-C_3N_4 have a lone pair of electrons and can change the electron configuration of the supported materials by interfacial charge redistribution. Studies on the Co_3O_4/g-C_3N_4 nanocomposite [94] and g-C_3N_4/Co_3O_4/α-Fe_2O_3 [95] have proved that a strong coupling interaction is formed at the interface between the g-C_3N_4 and the oxide, which acts as an effective electron transport channel and exposes more catalytically active sites, leading to outstanding OER performances with η_{20} values of 170 and 359 mV and Tafel values of 188 and 116 mV dec^{-1}, respectively. Following the synthesis of g-C_3N_4 NSs, CdSe quantum dots (QDs)/CN heterostructures are created through the successive ionic layer adsorption and reaction (SILAR) process (Figure 4b) [92]. As observed from LSV curves in a 0.1 M KOH electrolyte (Figure 4c), CdSe QDs/CN with 20 SILAR cycles presents outstanding OER activity with η_{10} of 200 mV, which is close to commercially available IrO_2 and surpasses g-C_3N_4 and CdSe QDs. Its Tafel slope of 109 mV dec^{-1} indicates more favorable OER kinetics (Figure 4d). Figure 4e illustrates the charge transfer at the interface of the heterostructure for overall water splitting (OWS) to develop H_2 and O_2 [92]. Another work [96] proposed a hierarchical carbon matrix decorated with nitrogen atoms (NC) as a support for obtaining high-performance ORR/OER electrocatalysts based on iron and nickel (Fe/Ni@N–C).

Among various carbon-based materials, CC is more widely used than g-C_3N_4 and NC for OER because of its excellent conductivity and high cost-effectiveness. The large specific surface area of CC enhances the contact between the electrode material and the electrolyte, and the constructed composites favor the thorough exposure of catalytic sites and charge/mass transfer, thus boosting electrochemical performance. Like a nickel foam (NF) substrate, active materials can be grown on it in situ to decrease the interface impedance. Both Chen et al. [83] (Figure 5a,b) and Kang et al. [84] used a grown-in situ $Ni(OH)_2$ nanosheet array on CC as a template. Subsequently, Kang et al. [84] employed magnetron sputtering technology to uniformly deposit tungsten nanoparticles onto $Ni(OH)_2$ nanosheets, successfully fabricating a heterostructure of W@$Ni(OH)_2$/CC. Chen et al. [83] fabricated three control samples for OER via mild sulfidation or selenidation: NiS_2, $NiSe_2$, and Se-doped NiS_2 (Se-NiS_2). Islam et al. [86] successfully developed a thin shell of NiO-$NiSe_2$ nanosheets on a template of in situ-grown TiN nanoarrays on CC (TiN@NiO-$NiSe_2$/CC) (Figure 5c) for high-performance OER.

By constructing a heterogeneous interface and adopting a 2D nanosheet morphology for the catalyst, the charge transfer, OER kinetics, and ion/gas transport processes are effectively accelerated. The large surface area with abundant heterogeneous interfaces synergistically enhances the OER activity. The conductive substrate facilitates electron transfer, while the in situ integration characteristics favor stable adhesion between the substrate and hybrid catalyst. Additionally, the electronic coupling effect of the heterostructure enhances both the OER kinetics and charge transfer performance and also drives the transformation of the catalyst surface into the active NiOOH layer. First-principal calculations reveal that the transformation to active NiOOH is strongly related to the bond strength [83]. For example, the Ni-S bonds in NiS_2 are too strong to generate NiOOH, and the Ni-Se bonds in $NiSe_2$ are too weak, causing Se to dissolve and leading to structural instability [83]. Meanwhile, the Ni-S bonds and Ni-Se bonds in Se-NiS_2 are modulated and moderate, resulting in the Se-NiS_2 surface's rapid conversion into NiOOH [83]. Consequently, Se-NiS_2 delivers improved OER activity and stability under alkaline conditions, with η_{50} of 343 mV [83]. During the surface's evolution into highly active NiOOH, anion leaching could occur. Anion leaching and adsorption onto the reconstructed surface is crucial for enhancing catalytic performance, as the disordered, porous, high surface area skeleton catalyst possesses numerous active sites that could be penetrated by the electrolyte and exhibit bulk activity. In addition, the defects could also promote the surface's transformation into highly active MOOH. For instance, Chen et al. [85] achieved a binder-free defect-rich NiFeP electrocatalyst (d-NiFeP/CC) by selectively etching Zn atoms from the Zn-NiFeP precursor. Acid etching primarily affected Zn atoms rather than Ni and Fe atoms, introducing surface defects. The introduction of defects not only facilitates the surface's evolution into highly

active NiOOH but also improves its stability. The d-NiFeP/CC exhibits a η_{10} value of only 185 mV with a Tafel slope of 24.56 mV dec^{-1} and stability of up to 100 h in alkaline OER. For OWS, d-NiFeP/CC displays a small cell voltage of 1.486 V to drive a current density of 10 mA cm^{-2}.

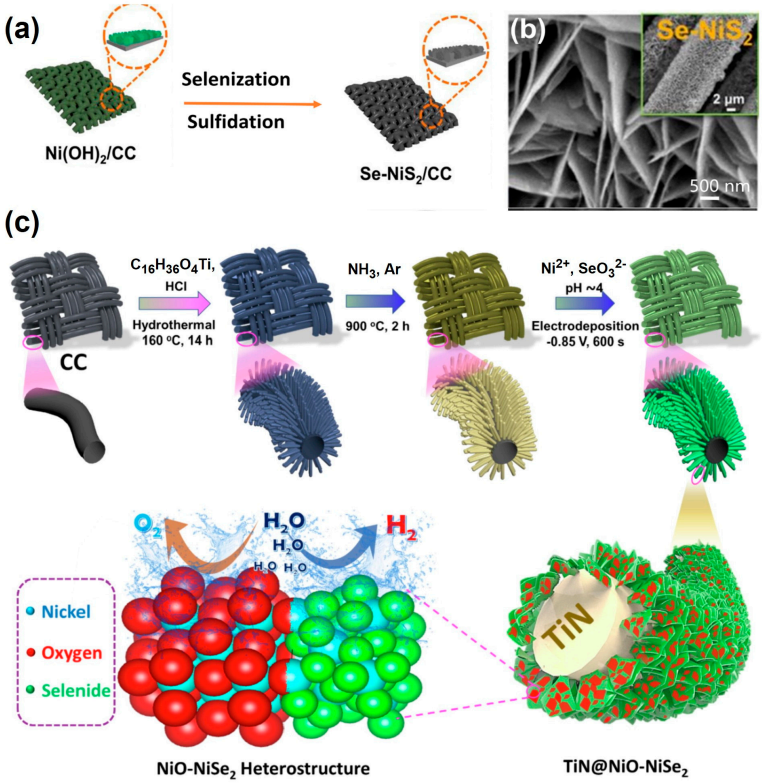


Figure 5. (**a**) Schematic illustration of fabricating Se-NiS_2 on CC and (**b**) SEM image of Se-NiS_2/CC [83]. All rights reserved. (**c**) Schematic design for the fabrication of TiN@NiO-$NiSe_2$ on CC [86].

In addition to sulfides/selenides, non-noble transition metal phosphides (TMPs) show superior or comparable OER activity to IrO_2/RuO_2 due to their unique and tunable electronic properties. The disadvantage of TMPs in accessible surface area can be compensated for by introducing conductive and porous carbon materials to improve mass/charge transfer efficiency. Numerous attempts have been made to develop effective TMP/carbon composites for OER. Amongst various TMP phases, multi-metal centered TMPs such as alloyed FeCo phosphides exhibit enhanced OER activity [97]. Liu et al. [98] fabricated a composite of NiCoFe-P/C with 0-dimensional (0D) NiCoFe-P QSs supported by 2D N-doped C (Figure 6a,b) via the carbonization and phosphorization of NiCoFe-ZIF precursors. The prepared NiCoFe-P/C 0D/2D heterostructure had excellent alkaline OER activity with η_{100} of 257 mV (Figure 6c). Safer substitutes, such as phytic acid (PA), are being explored to replace toxic phosphorus sources, such as NaH_2PO_2, $P(SiMe_3)_3$, tri-noctylphosphine, and elemental phosphorus. Wang et al. [87] initiated a one-pot strategy for the green, facile, and mass production of a highly active and stable catalyst for OER/ORR/HER through the preparation of Fe/Co cross-linked tofu gel and its subsequent pyrolysis (Figure 6d). Despite the free use of additional N/P precursors or pore-forming agents, the as-prepared materials comprised highly dispersive FeCo-rich phosphide nanoparticles and a porous N,P co-doped carbon framework inherited from the tofu skeleton (Figure 6e,f). The as-fabricated electrocatalysts exhibited remarkably enhanced trifunctional activities, with η_{10} values of 281 mV vs. 341 mV (RuO_2), 353 mV (Fe_2P@NPC), 376 mV (Co_2P@NPC), and 453 mV (NPC), along with better long-term stability than the benchmark RuO_2 catalyst. Furthermore, the as-constructed alkaline electrolyzer required only a small voltage of

1.55 V@10 mA cm^{-2}, which outperforms nearly every biomass-derived electrocatalyst ever reported, and that of noble metal catalyst-based electrolyzers (1.72 V@10 mA cm^{-2} for Pt/C-RuO_2) (Figure 6g) [87]. A similar green synthesis strategy was employed by Wang et al. [88] (Figure 6h,i) and Zhang et al. [91], who used biomass-derived N-containing chitosan as the carbon source and PA as the precursor of both phosphorus and carbon. After being stirred to form a chelated structure, freeze-dried, and carbonated, the obtained dual-TMP nanoparticles embedded in (N, P) co-doped porous carbon exhibited excellent alkaline OER performances. $FeCoP_2$@NPPC [88] and $Ni_{0.8}Fe_{0.2}P$-C [99] require overpotentials of 236 and 242 mV for OER reaching 10 mA cm^{-2} in a 1.0 M KOH solution, respectively. The latter can work stably for over 100 h [99].

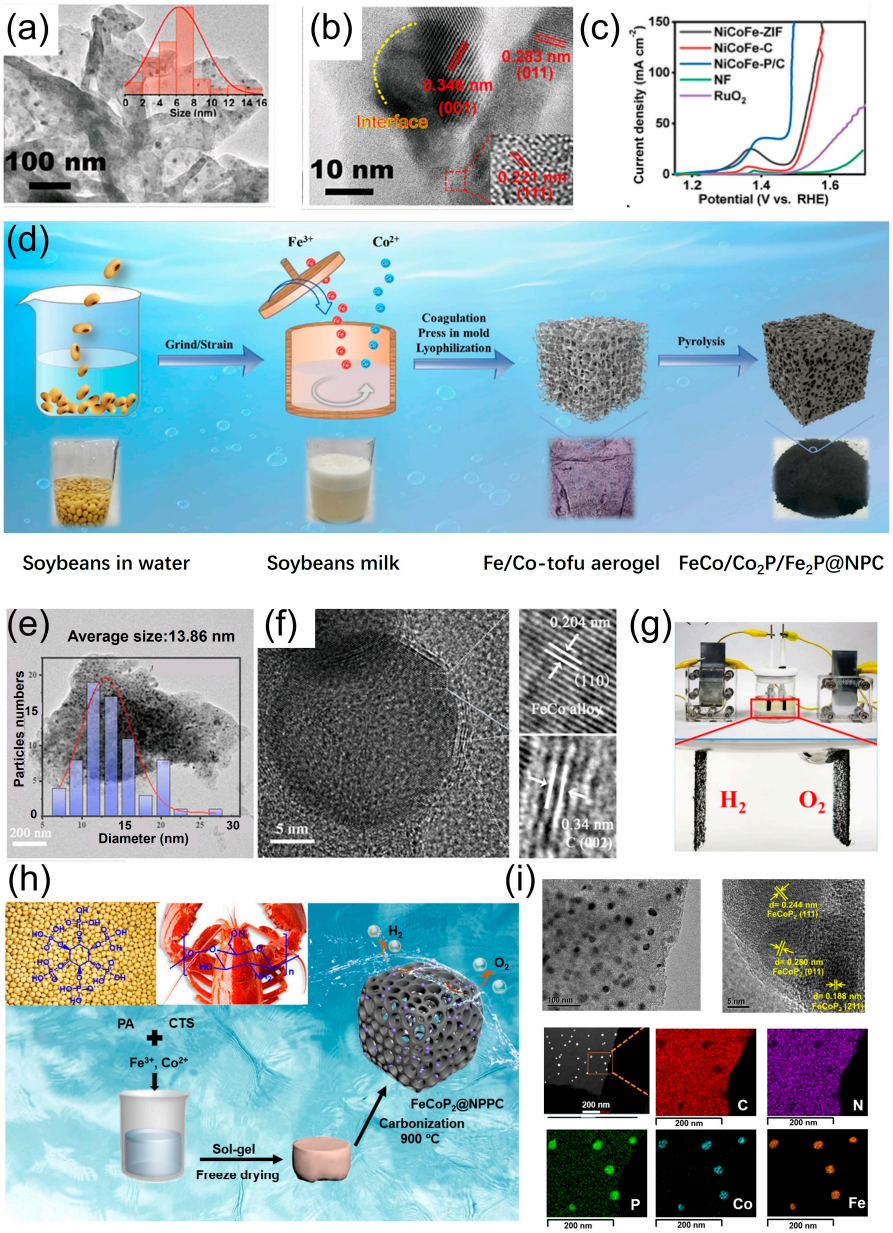


Figure 6. (**a**) TEM (inset: the particle size distribution), (**b**) HRTEM images, and (**c**) alkaline OER performances of NiCoFe-P/C [98]. (**d**) Schematic illustration of the preparation procedure of FeCo/Co_2P/Fe_2P@NPC. (**e**) TEM image of FeCo/Co_2P/Fe_2P@NPC (inset: the size distribution of nanoparticles), and (**f**) HRTEM images of one nanoparticle. (**g**) Digital photo showing the operating state of the as-constructed self-powered overall water-splitting system [87]. (**h**) Synthesis route and (**i**) TEM and HRTEM images of $FeCoP_2$/NPPC [88].

Carbon paper (CP) [100–102], rGO [103], and graphene [104–106] are also used as the support. The heterostructure directly grows on CP with a high surface area and excellent conductivity, ensuring outstanding electrode performance. For example, a $Ni_{0.70}Fe_{0.10}V_{0.20}S_2$ core encapsulated within an amorphous NiFe hydroxide shell supported on CP presents excellent OER performance in a 1.0 M KOH electrolyte, with η_{10} of 204 mV and a Tafel slope of 39 mV dec^{-1} [100]. These superior characteristics are primarily attributed to the synergistic effects between the core–shell structure, the high electronic conductivity of the core, the presence of additional active sites on the amorphous shell surface, and the strong adhesion between the active materials and conductive support. The incorporation of metallic V expedites electron transfer during the OER process, while Fe doping introduces 3d states near the Fermi level, thereby enhancing electronic conductivity. The in situ-generated amorphous iron hydroxide possesses many high-valent active sites, favoring the adsorption of negatively charged reaction-involved species like OH^- and $HO_2{}^-$.

3.2.2. At HCD

Although much progress has been made in developing LCD OER electrocatalysts, most electrocatalysts perform well only at relatively low current densities, which do not meet the requirements of industrial electrochemical applications. For practical production applications, stable operation at high current densities ($\geq$500 mA cm^{-2}) is imperative [12]. At HCD, the accumulation of a large number of bubbles will greatly slow down the charge and mass transfer of the electrode, reduce the exposure of the active site, and lead to high overpotential, which sets stricter demands on HCD OER electrocatalysts. The high surface area and high porosity of carbon-based materials favors the diffusion of oxygen molecules [82].

Studies have shown that grown-in situ active OER materials on CC with honeycomb-like morphologies composed of nanosheets [89], nanoneedle arrays [75], and nanofollowers assembled by nanosheets/nanowires [107,108] have excellent HCD OER performance. As in the LCD scenario, CC self-supported multi-metal center composites usually perform better than single-metal systems [109]. That may be because the differences in the enthalpy values of the metal centers induce the formation of the heterojunction, causing the rearrangement of interface electrons and resulting in electron-enriched and electron-deficient regions. This facilitates the adsorption of H^+ and OH^-/H_2O, thereby promoting HER and OER activity [110]. For instance, Qin et al. [89] used in situ-grown V-MOF on CC as the precursor, followed by the introduction of Ni and Fe components through electrodeposition, synchronized phosphorization, and selenization treatments, ultimately yielding a Ni-Fe-V ternary metal phosphoselenide composite ($NiV_2P/FeSe$@CC). The obtained hierarchical porous 3D CC-supported honeycomb-like composite delivered η_{10} and η_{200} of only 168 and ~282 mV in an alkaline environment, respectively. The assembled electrolyzer required a voltage of 1.53 V at 10 mA cm^{-2} and exhibited outstanding stability for 160 h at 100 mA cm^{-2}. Also, the in situ-grown mesoporous $CuMn_{0.5}Co_2O_4$ nanoneedle array on CC ($CuMn_{0.5}Co_2O_4$/CC) achieved η_{10} and η_{200} of 189 and ~327 mV in 1 M KOH, respectively, outperforming Co_3O_4/CC, $CuCo_2O_4$/CC, and some other single-metal oxide systems [90]. Similarly, the CC self-supported follower-like hierarchical dual-metal sulfides, e.g., an FeS/Co_3S_4/CC heterostructure [107] or a non-metal-doped sulfide, e.g., V,P-CoS_2/CC [108], also showed improved performance compared with the single component.

Zhang et al. [82] compared the effect of different carbon substrates on catalytic performance (Figure 7a). They found that C_3N_4 was a better substrate than CNT and GO, possibly due to the presence of N. In addition, C_3N_4 and P-doped C_3N_4 (C_3N_4-P) loaded on NF displayed little catalytic activity below 1.55 V. Although Ni phosphide may also form in P-doped C_3N_4, in which Ni is from the NF support, the amount of Ni phosphide produced is insufficient to catalyze the OER. From the experiments described above, it can be concluded that using $K_3Fe(CN)_6$, C_3N_4, NaH_2PO_2, and NF is critical for the superior performance of the FeNi-C_3N_4-P catalyst. To synthesize the FeNi-C_3N_4-P catalyst, FeNi

PBA was first produced on a NF substrate in the presence of C_3N_4. The obtained material was then subjected to a high-temperature phosphating process (Figure 7c). As expected, the resulting FeNi-C_3N_4-P catalyst exhibits excellent OER activity. It shows a small Tafel slope of 40.4 mV dec^{-1}, a low overpotential of 235 mV at 100 mA cm^{-2}, and remarkable stability (Figure 7b) [82].

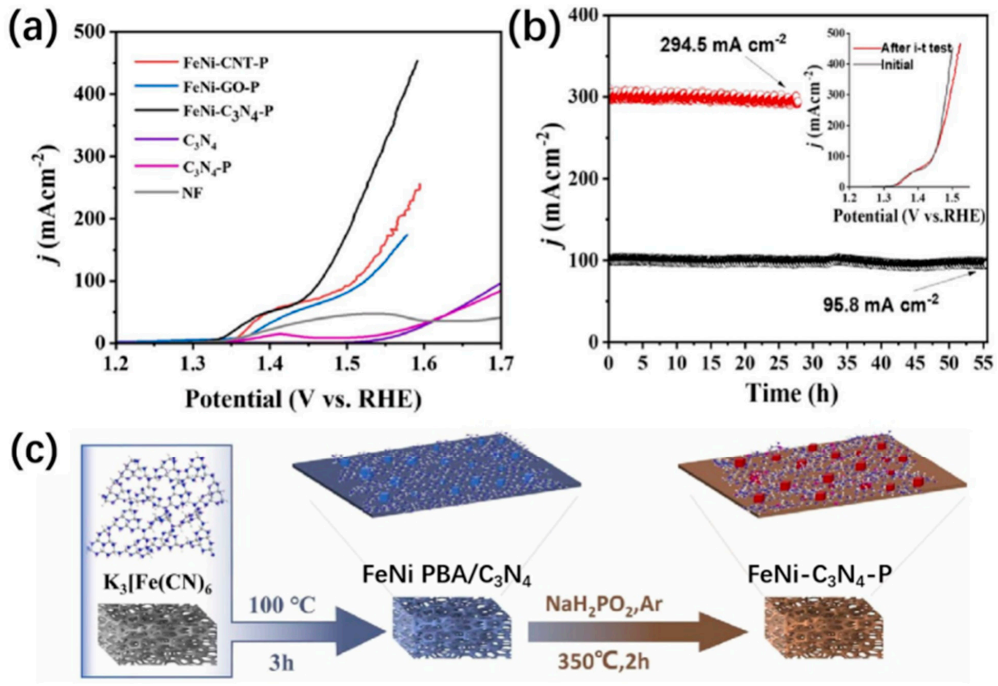


Figure 7. (**a**) OER LSV curves. (**b**) i-t chronoamperometric tests for FeNi-C_3N_4-P at overpotentials of 245 mV and 320 mV for 28 h and 55 h in turn. Inset is the comparison of polarization curves of FeNi-C_3N_4-P after the i-t test. (**c**) Schematic illustration for the formation of NF-supported FeNi-C_3N_4-P [82].

In addition to the common *n*D/3D hierarchical structure [111], the *n*D/0D hierarchical structure has also been developed for HCD OER. Carbon quantum dots (CQDs), characterized by their small nanoscale dimensions, effectively prevent corrosion and extend stability [112]. Additionally, CQDs possess favorable hydrophilic and aerophobic properties, aiding in regulating the electrolyte/catalyst interface and facilitating the rapid ingress of reactants and smooth detachment of oxygen bubbles to boost HCD OER further. When used in constructing the composites, CQDs pass on excellent hydrophilic and aerophobic properties to the connected active materials. Recently, Pan et al. [91] reported an in situ activation of Fe-NiOOH nanoclusters on CQDs (Fe-NiOOH/CQDs) to achieve HCD OER. After directly dropping a NiFe-CQD ink solution on the CP, the prepared working electrode demonstrated an in situ self-activation process in OER. It took 50 cycles of CV activation to fulfill the almost complete evolution of MO to a M-OOH active species so that the system reached optimal activity (Tafel slope: 35 mV dec^{-1}, η_{10} = 199 mV, η_{1000} = 450 mV with a turnover frequency of up to 5.4 s^{-1}).

3.3. Carbon-Based Core–Shell Composite

Although carbon substrates can effectively improve conductivity, direct exposure of active materials such as metal compounds to electrolytes can lead to the inevitable corrosion dissolution of metals and structural collapse, resulting in poor stability. A core–shell structure is widely used to improve catalyst stability [113–116]. Fabricating a carbon shell has the following advantages: (i) conductivity can be greatly improved; (ii) the electronic interaction between the carbon shell and the encapsulated metal can promote the activation of catalytic sites and improve intrinsic activity; (iii) carbon coating

can protect encapsulated metals from corrosion caused by direct contact with electrolytes, effectively enhancing the stability of the structure. Based on this, extensive research has been conducted on carbon-coated structures for high-performance OER [117]. Note that a suitable thickness of carbon shell is required for optimal OER performance.

3.3.1. At LCD

As previously mentioned, TMPs deliver superior OER activity. Great efforts have been made to develop not only TMP/carbon but also TMPs@carbon [118,119] electrocatalysts, creating a viable alternative to IrO_2/RuO_2-based electrocatalysts. Structural regulation is essential for realizing efficient and stable OER catalysis. Lv et al. [120] reported an effective strategy to enhance the performance of core–shell Co_2P@NC electrocatalysts via secondary metal (e.g., Fe, Ni, Mo, Al, Mn) doping (referred to as M-Co_2P@M-N-C). Under a hydrogen atmosphere, the transition metal-doped organic–inorganic phosphonate cobalt (tm-melamine/TM-HEDP-Co) precursor introduces secondary metal into the Co_2P core during high-temperature pyrolysis, simultaneously forming a M-N-C shell with highly active M-N_4 sites. The addition of Fe enhances the activity of the Co_2P core in HER/OER by optimizing the electronic structure, while well-constructed Fe-N_4 active sites in the Fe-N-C shell effectively promote OER/ORR. Thereby, the Fe-Co_2P@Fe-N-C electrocatalyst exhibits the best catalytic activity among the M-Co_2P@M-N-C electrocatalysts, achieving a current density of 10 mA cm^{-2} at 1.58 V for OWS (Table 2). This outstanding performance is closely associated with the subtle synergistic effect between the highly active components (the Fe-doped Co_2P core and Fe-N-C shell) and the durable carbon shell. The stable Fe-N-C shell plays a vital role in rapid electron transport and effectively prevents the corrosion of the Fe-Co_2P core in alkaline electrolytes.

Carbon-encapsulated alloys, oxides, carbides, and sulfides (alloys@carbon [60], oxides@carbon [97], carbides@carbon [121]), sulphides@carbon [122]) are other representative core–shell electrocatalysts for OER. Alhakemy et al. [123] employed a facile one-step approach to fabricate a composite with $CoFe_2O_4$ (CFO) as the core and carbon spheres (CSs) as the shell. The incorporation of CFO introduced additional catalytic active sites for OER, endowing the CFO/CS with low overpotential and charge transfer resistance during the OER process. After extended stability tests, the CFO@CSs hybrid retained its spherical structure, with CFO nanoparticles uniformly dispersed within the CSs, demonstrating excellent structural stability. Abbas et al. [121] encapsulated iron carbide (Fe_3C) nanoparticles within a N-doped graphite carbon shell through a straightforward carburizing ion process. The graphite carbon shell significantly enhanced the activity and stability of the Fe_3C@C and Fe_3C@C-N electrocatalysts compared to the bare Fe_3C nanoparticles. Fe_3C@C-N exhibited markedly improved activity and stability in OER, attributable to the synergistic effect between the active core and the stabilizing shell structure. Note that the Fe-N sites in Fe_3C@C-N are not OER-active centers. However, N doping increased the quantity of Fe_3C in the catalyst and hence surpassed the overall performance of Fe_3C@C.

Table 2. Comparison of core–shell carbon-based materials for OER and water splitting by overpotential (η, mV); current density (j, mA cm^{-2}); Tafel slope (TS, mV dec^{-1}); and stability (Sta., h).

Materials	Morphology	OER			Water Splitting [a]		Electrolyte	Ref.
		η at j	TS	Sta.	U at j	Stab.		
Fe-Co_2P@Fe-N-C	Core–shell nanostructure; Fe-doped Co_2P core and Fe-N-C shell	300@10	79	24@50	1.58@10	10	1 M KOH	[120]
CFO@CSs	Carbon-coated spherical structure; core: $CoFe_2O_4$	390@10	57.75	6@10	1.87@10	20@10	1 M KOH	[123]
Ni@PMMA-BM	Carbon-coated honeycomb-like structure	263@10	34	28@10	N.A.	N.A.	1 M KOH	[124]

Table 2. *Cont.*

Materials	Morphology	OER			Water Splitting [a]		Electrolyte	Ref.
		η at j	TS	Sta.	U at j	Stab.		
Fe_3C@C–N	Core–shell nanostructure; core: Fe_3C; shell: nitrogen-doped graphene-like layers	469@10	89	13.8@1.7 V	N.A.	N.A.	0.1 M KOH	[121]
Fe/Fe_3C@C/CNT	Carbon-coated Fe/Fe_3C nanoparticles anchored to CNTs	292@10	29	12@50	N.A.	N.A.	1 M KOH	[125]
$Ni_{0.70}Fe_{0.10}V_{0.20}S_2$-AH/CP	Core–shell trimetallic heterostructures grown on carbon paper	204@10	39	24@10	N.A.	N.A.	1 M KOH	[100]
CoP/DCS	CoP nanoparticles encapsulated in a rich-defect carbon shell	251@10	81.6	72	1.49@10	24@10	1 M KOH	[117]
S/N-CMF@$Fe_xCo_yNi_{1-x-y}$-MOF	Core–shell nanostructure; core: S/N-doped carbon mesoporous fibers; shell: ternary metal centers MOFs	296@10 377@200	53.5	100@10	N.A.	N.A.	1 M KOH	[68]
(V_2O_3−$CoFe_2O_4$)@C/NF [a]	V_2O_3-decorated spinel $CoFe_2O_4$ with carbon-encapsulated nanosheets grown on NF	226@10 310@500	56	80@500	1.53@10 1.89@150	80@100	1 M KOH	[18]

[a]: The anode and cathode use the same electrode in WOS with the exception of using Pt/C as the anode. N.A.: Not available.

Besides the composition (C, C-N, C-P, and other combinations), the thickness of the carbon coating is also a key factor in regulating the electron penetration effect and catalytic performance for interfacial heterogeneous catalytic reactions. Although carbon coating can improve catalytic stability, an extremely thick carbon layer can weaken the electron penetration effect and hinder the improvement of intrinsic activity. DFT calculations reveal that as the graphene layer of the carbon shell increases, the electron transfer from the metal core to the outermost carbon shell rapidly decreases [124]. Therefore, it is necessary to precisely control the thickness of the carbon coating through a convenient and effective preparation method, which is the key to optimizing the electron penetration effect and achieving a balance between activity and stability.

The differences in carbon content among different carbon sources significantly impact the growth process of heterostructures. Metal–organic compounds with high carbon content can promote the formation of carbon coatings, while inorganic metal compounds with lower carbon content tend to create thin or no carbon coatings. Using iron acetylacetonate ($Fe(C_5H_7O_2)_3$), ferrous carbonate ($FeCO_3$), and iron phthalocyanine ($C_{32}H_{16}FeN_8$) as both iron and carbon precursors, Gao et al. [125] found that in situ fast carbonization of acetylacetonate iron based on CNT-induced rapid microwave heating can obtain Fe/Fe_3C-A@CNT with a suitable carbon layer thickness and hence effectively prevent the aggregation of iron-based compounds and promote the uniform dispersion of Fe/C heterostructures (Figure 8a). A higher carbon content in metal–organic compounds makes it easier to form a carbon coating on the metal surface during carbonization, as observed with acetylacetonate iron and phthalocyanine iron, where the thickness is directly proportional to the carbon content in the metal source [125]. Experimental results demonstrate that an Fe/Fe_3C-A@CNT sample with a surface carbon layer of ~1.77 nm thickness exhibits a lower overpotential (η_{10} = 292 mV) and a smaller Tafel slope (29 mV dec^{-1}) than samples with thicker carbon layers (>9 nm) (Fe/Fe_3C-P@CNT and FeACAO@CT) and samples without a carbon layer (Fe/Fe_3C-C@CNT) [125]. In another work, Zhao et al. [124] found that the length of ball milling treatment (Figure 8d–f,h,i) also affected the thickness of the carbon shell when they employed a mechanochemical approach with plastic waste

as the precursors to synthesize Ni@C electrocatalysts with tunable core–shell structures, octahedral-like crystal (OLC) morphology, and abundant surface defects. The ball milling process effectively facilitates the uniform dispersion of the metal precursor within the plastic matrix, resulting in an adjustable active core–shell structure. The metal species, encapsulated by carbon shells derived from plastic, are uniformly embedded in a highly porous carbon support. OER electrocatalysts based on transition metals (such as Co, Ni, Mn, and Fe) @C exhibited significantly enhanced OER kinetics than commercial IrO_2, with performance following the order Ni > Co ≈ Fe > Mn. A carbon shell with a controllable thickness alters the permeability of reactants/electrolytes by eliminating specific adsorption sites on the metal surface. The optimal Ni@PMMA-BM prepared by the mechanochemical method achieved a current density of 10 mA cm^{-2} at 263 mV in 1.0 M NaOH. XRD patterns of the Ni@PMMA-BM samples sintered at different temperatures (Figure 8k) demonstrate that as the temperature increased, Ni_3C and Ni oxides gradually disappeared and finally all converted to metallic Ni. That is, ball milling promotes the physical mixing and full contact of the carbon precursor with nickel nitrate and also the in situ formation of a carbon layer outside the Ni particles during the annealing process under N_2 at 850 °C (Figure 8k).

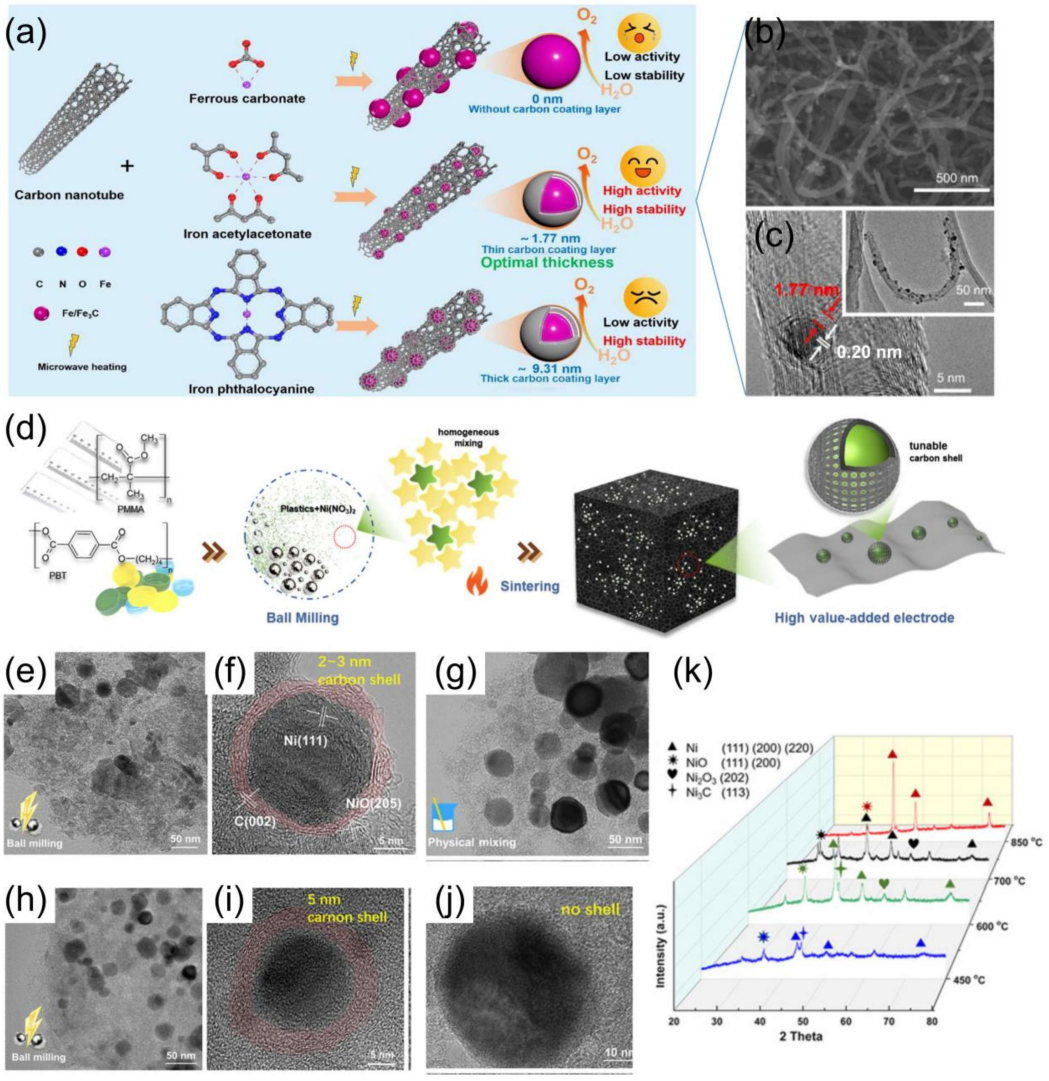


Figure 8. (**a**) Schematic illustration of fabricating Fe/Fe_3C-C@CNT, Fe/Fe_3C-A@CNT, and Fe/Fe_3C-P@CNT [125]. (**b**) SEM and (**c**) TEM of Fe/Fe_3C-A@CNT [125]. (**d**) Schematic illustration for the mechanochemical synthesis of the metal/metal oxides@carbon [124]. TEM images of (**e**,**f**) Ni@PMMA-BM (1 h), (**h**,**i**) Ni@PMMA-BM-3 h, and (**g**,**j**) Ni@PMMA-PM. "3 h" represents the ball milling treatment [124]. (**k**) XRD of Ni@PMMA-BM at 450 °C–850 °C [124].

3.3.2. At HCD

Similar to OER at LCD [65], a suitable carbon shell thickness is required for optimal OER performance at HCD. An increase in carbon layer thickness and crystallinity could attenuate the activity of potential active metal sites and hinder electron transport, as confirmed by Wang et al. [126]. They found that the synthesized high-entropy alloy (HEA) CoNiCuMnAl@C nanoparticles derived from multi-metallic MOFs [126] at a calcination temperature of 900 °C had a denser carbon layer and higher crystallinity and showed worse catalytic performance than those with a thinner carbon layer. The optimal CoNiCuMnAl@C/NF (deposited film on NF via electrophoretic deposition) with a novel core–shell nanostructure (core: a face-centered cubic HEA, shell: an extremely thin carbon layer) substantially promoted OER in 1.0 M KOH, exhibiting η_{200} of ~279 mV. Immersion in a 1.0 M KOH solution for up to 30 h at 200 mA cm^{-2} demonstrated its enduring OER stability. For comparison, by depositing CoNiCuMnAl@C on commercial carbon paper, the electrode achieved a current density of 100 mA cm^{-2} at 368 mV [126]. The protection role of the carbon layer at HCD was also confirmed by Kong et al. [119]. They fabricated a 3D self-branched hierarchical nanostructure composed of ultra-small CoP nanoparticles embedded into N,P-co-doped carbon nanotubes knitted hollow nanowall arrays (CoP@NPCNTs HNWAs) on carbon textiles (CTs) via a carbonization–phosphatization process. It exhibited superior electrocatalytic activity and stability in alkaline solutions [119]. It was capable of running for 200 h under the corresponding potential at 100 mA cm^{-2}. The assembled CoP@NPCNTs/CTs||CoP@NPCNTs/CTs electrolyzer achieved a high current density of 200 mA cm^{-2} at a low cell voltage of 1.78 V for OWS [119].

Carbon-encapsulated alloys/oxides/sulfides nanosheets grown on NF also show great potential for alkaline OWS at HCD [17,18]. For instance, trimetallic (Fe, Co, Ni) spinel/carbon/nickel foam ($FeCoNiO_x$/C/NF) electrodes with 3D network structures have an extremely low Tafel slope of 21 mV dec^{-1} at a current density of 10 mA cm^{-2} in 1.0 M KOH due to superhydrophilic/superaerophobic properties [127]. The optimal $FeCoNiO_x$/C/NF reaches a high current density of 500 mA cm^{-2} at a low overpotential of 325 mV with long-term stability of 250 h.

In addition to the aforementioned carbon-supported and carbon-encapsulated structures, a reverse carbon-core@shell structure has been developed. A novel OER electrocatalyst of MOFs with ternary metal centers coating S/N-doped carbon mesoporous fibers (S/N-CMF@$Fe_xCo_yNi_{1-x-y}$-MOF) (Figure 9a) has been reported recently [68]. In the last step of the cation exchange reaction, some Ni^{2+} in Ni-MOF was replaced by Fe^{2+}/Co^{2+}, and the S/N-CMF@Ni-MOF catalyst ultimately transformed into S/N-CMF@$Fe_xCo_yNi_{1-x-y}$-MOF, which retained the original hollow fiber structure. The process was accompanied by the shift of the Ni *d*-band center of Fe/Co-doped γ-NiOOH on the surface of Ni-MOF towards the Fermi level. That is, the doped Fe and Co atoms cooperatively modulated the electronic structure of Ni sites, thereby increasing the number of antibonding states and the energy of valence states and inducing improved OER performances. The enhanced intrinsic activity was conferred by the ternary metal component and the hollow S/N-CMF matrix (Figure 9b,c).

S/N-CMF@$Fe_xCo_yNi_{1-x-y}$-MOF, pasted on CP as the working electrode, exhibits η_{10} and η_{200} of 296 and ~377 mV (Figure 9d), respectively, with a Tafel slope of 53.5 mV dec^{-1}.

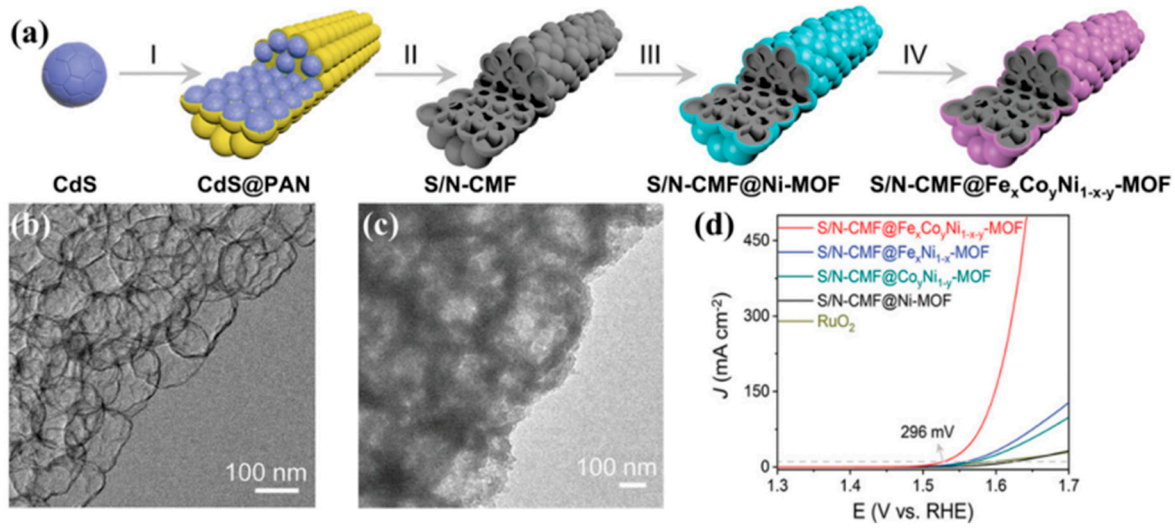


Figure 9. (**a**) Illustration of the synthetic process for creating S/N-CMF@$Fe_xCo_yNi_{1-x-y}$-MOF. TEM images of (**b**) S/N-CMF and (**c**) S/N-CMF@$Fe_xCo_yNi_{1-x-y}$-MOF. (**d**) LSV polarization curves in a 1.0 M KOH solution [68].

4. Conclusions and Outlook

OER plays a vital role in the performance of a series of green energy storage and conversion devices. The fabrication of cost-effective OER electrocatalysts is highly desirable. This review summarizes the recent progress in carbon-based composites for alkaline OER electrocatalysts from the perspective of design, fabrication, and application.

Some metal-free COF- and POP-based materials, such as TDA-Trz-POP with N- and S-rich surfaces [27], present comparable alkaline OER activity to IrO_2/RuO_2. The g-C_3N_4 itself is active in OER. As the substrate or shell, it cooperates with the supported or encapsulated materials to boost the OER. Besides g-C_3N_4, the widely employed carbon-based materials include biomass-derived porous carbon, rGO, CC, and CNT. Carbon-based materials-supported/encapsulated active materials, e.g., transition metal oxides, hydroxides/LDHs, phosphides, sulfides, selenides, carbides, and alloys, are highly efficient for OER. Structural features, including crystal phases and composition, are closely related to the preparation methods employed, and most of the present carbon-based materials are obtained via high-temperature calcination. A green, affordable, simple, low-cost, and easy large-scale preparation method is urgently needed. Moreover, the thickness of the carbon layer has been confirmed to affect OER activity at both LCD and HCD strongly. Therefore, in addition to assessing the currently used mechanochemically assisted synthesis methods [124] or selecting appropriate types of metal–organic salts [125], future work could focus on developing other facile methods for controlling the thickness of the carbon layer. Convenient methods should also be developed to improve the stability of carbon-based electrocatalysts and avoid degradation [128].

As is well known, the four-electron oxidation reaction involved in OER requires continuous intermediate valence state change steps, making the kinetics of the catalytic cycle very complex and causing slow overall catalytic kinetics [19,129–131]. Gaining a deep understanding of the working mechanism of OER electrocatalysts, including the role of carbon-based materials in alkaline OER, is challenging. Future research on in situ experimental techniques and accurate calculation methods to deal with the complex reaction environment is encouraged. An accurate calculation method would include active learning optimization strategies that integrate uncertainty. Various uncertainty factors strongly influence the efficiency of the data-driven method in developing new materials. Therefore, it is important to effectively evaluate uncertainty and use it to develop data-driven strategies to achieve the rational design of new OER electrocatalysts. In addition, developing universal machine learning methods can further save design costs.

To summarize, future work should focus on methods of designing inexpensive electrocatalysts with high activity and stability under complex and harsh reaction conditions.

Author Contributions: Conceptualization, X.-R.S. and S.X.; validation, P.W., H.Y. and M.Z.; formal analysis, C.G., P.W., H.Y. and M.Z.; investigation, C.G., P.W. and H.Y.; resources, C.G., P.W., H.Y., M.Z. and X.-R.S.; data curation, C.G., P.W. and H.Y.; writing—original draft preparation, C.G.; writing—review and editing, X.-R.S. and S.X.; supervision, X.-R.S. and S.X.; project administration, X.-R.S.; funding acquisition, X.-R.S. and S.X. All authors have read and agreed to the published version of the manuscript.

Funding: This work was financially supported by the Shanghai Natural Science Foundation (23ZR1425500), Shanghai Sailing Program (20YF1416100), Shanghai Local Universities Capacity Building Project of Science and Technology Innovation Action Program (21010501700), and Class III Peak Discipline of Shanghai—Materials Science and Engineering (High-Energy Beam Intelligent Processing and Green Manufacturing).

Institutional Review Board Statement: Not applicable.

Informed Consent Statement: Not applicable.

Data Availability Statement: Data are contained within the article.

Acknowledgments: The authors are very grateful to the Shanghai Science and Technology Commission for the support.

Conflicts of Interest: The authors declare no conflicts of interest.

References

1. Fan, R.; Liu, C.; Li, Z.; Huang, H.; Feng, J.; Li, Z.; Zou, Z. Ultrastable Electrocatalytic Seawater Splitting at Ampere-Level Current Density. *Nat. Sustain.* **2024**, *7*, 158–167. [CrossRef]
2. Gu, J.; Li, L.; Xie, Y.; Chen, B.; Tian, F.; Wang, Y.; Zhong, J.; Shen, J.; Lu, J. Turing Structuring with Multiple Nanotwins to Engineer Efficient and Stable Catalysts for Hydrogen Evolution Reaction. *Nat. Commun.* **2023**, *14*, 5389. [CrossRef] [PubMed]
3. Shi, H.; Wang, T.; Liu, J.; Chen, W.; Li, S.; Liang, J.; Liu, S.; Liu, X.; Cai, Z.; Wang, C.; et al. A Sodium-Ion-Conducted Asymmetric Electrolyzer to Lower the Operation Voltage for Direct Seawater Electrolysis. *Nat. Commun.* **2023**, *14*, 3934. [CrossRef]
4. Magnier, L.; Cossard, G.; Martin, V.; Pascal, C.; Roche, V.; Sibert, E.; Shchedrina, I.; Bousquet, R.; Parry, V.; Chatenet, M. Fe-Ni-Based Alloys as Highly Active and Low-Cost Oxygen Evolution Reaction Catalyst in Alkaline Media. *Nat. Mater.* **2024**, *23*, 252–261. [CrossRef] [PubMed]
5. Yu, Z.-Y.; Duan, Y.; Feng, X.-Y.; Yu, X.; Gao, M.-R.; Yu, S.-H. Clean and Affordable Hydrogen Fuel from Alkaline Water Splitting: Past, Recent Progress, and Future Prospects. *Adv. Mater.* **2021**, *33*, 2007100. [CrossRef] [PubMed]
6. Ganguly, A.; McGlynn, R.J.; Boies, A.; Maguire, P.; Mariotti, D.; Chakrabarti, S. Flexible Bifunctional Electrode for Alkaline Water Splitting with Long-Term Stability. *ACS Appl. Mater. Interfaces* **2024**, *16*, 12339–12352. [CrossRef] [PubMed]
7. Guo, J.X.; Zheng, Y.; Hu, Z.P.; Zheng, C.Y.; Mao, J.; Du, K.; Jaroniec, M.; Qiao, S.Z.; Ling, T. Direct Seawater Electrolysis by Adjusting the Local Reaction Environment of a Catalyst. *Nat. Energy* **2023**, *8*, 264–272. [CrossRef]
8. Retuerto, M.; Pascual, L.; Torrero, J.; Salam, M.A.; Tolosana-Moranchel, Á.; Gianolio, D.; Ferrer, P.; Kayser, P.; Wilke, V.; Stiber, S.; et al. Highly Active and Stable OER Electrocatalysts Derived from Sr_2MIrO_6 for Proton Exchange Membrane Water Electrolyzers. *Nat. Commun.* **2022**, *13*, 7935. [CrossRef] [PubMed]
9. Karmakar, A.; Senthamaraikannan, T.G.; Baasanjav, E.; Bandyopadhyay, P.; Jin, B.; Park, Y.S.; Lim, D.-H.; Jeong, S.M. Surface Hydroxyl Group-Enriched Nickel Cobalt Molybdate Hydrate for Improved Oxygen Evolution Activity in an Anion Exchange Membrane Water Electrolyzer. *Appl. Catal. B* **2023**, *328*, 122504. [CrossRef]
10. Shimada, H.; Yamaguchi, T.; Kishimoto, H.; Sumi, H.; Yamaguchi, Y.; Nomura, K.; Fujishiro, Y. Nanocomposite Electrodes for High Current Density over 3 A Cm^{-2} in Solid Oxide Electrolysis Cells. *Nat. Commun.* **2019**, *10*, 5432. [CrossRef]
11. Dionigi, F.; Zeng, Z.; Sinev, I.; Merzdorf, T.; Deshpande, S.; Lopez, M.B.; Kunze, S.; Zegkinoglou, I.; Sarodnik, H.; Fan, D.; et al. In-Situ Structure and Catalytic Mechanism of NiFe and CoFe Layered Double Hydroxides during Oxygen Evolution. *Nat. Commun.* **2020**, *11*, 2522. [CrossRef] [PubMed]
12. Zhai, P.; Wang, C.; Zhao, Y.; Zhang, Y.; Gao, J.; Sun, L.; Hou, J. Regulating Electronic States of Nitride/Hydroxide to Accelerate Kinetics for Oxygen Evolution at Large Current Density. *Nat. Commun.* **2023**, *14*, 1873. [CrossRef] [PubMed]
13. He, Z.; Zhang, J.; Gong, Z.; Lei, H.; Zhou, D.; Zhang, N.; Mai, W.; Zhao, S.; Chen, Y. Activating Lattice Oxygen in NiFe-Based (Oxy)Hydroxide for Water Electrolysis. *Nat. Commun.* **2022**, *13*, 2191. [CrossRef] [PubMed]
14. Huang, M.; Shi, X.-R.; He, X.; Zhang, X.; Cao, F.; Wang, P.; Sun, C.; Xu, S.; Zhang, M. Electronically Regulated FeOOH/c-$NiMoO_4$ with Hierarchical Sandwich Structure as Efficient Electrode for Oxygen Evolution and Hybrid Supercapacitors. *Electrochim. Acta* **2022**, *427*, 140884. [CrossRef]

15. Yan, Y.; Zhang, J.-Y.; Shi, X.; Zhu, Y.; Xia, C.; Zaman, S.; Hu, X.; Wang, X.; Xia, B.Y. A Zeolitic-Imidazole Framework-Derived Trifunctional Electrocatalyst for Hydrazine Fuel Cells. *ACS Nano* **2021**, *15*, 10286–10295. [CrossRef] [PubMed]
16. Xu, M.; Jiang, H.; Liu, Y.; Xu, L.; Jiang, H.; Guo, Y.; Guo, Y.; Xuan, K.; Wang, L.; Ge, Q.; et al. Self-Supported Sheet-like Bi_2O_3 Electrodes for Co-Electrolysis of CO_2 Conversion and Cl^- Upgrading. *Sep. Purif. Technol.* **2024**, *339*, 126592. [CrossRef]
17. Wang, Z.; Qian, G.; Yu, T.; Chen, J.; Shen, F.; Luo, L.; Zou, Y.; Yin, S. Carbon Encapsulated $FeWO_4$-Ni_3S_2 Nanosheets as a Highly Active Catalyst for Overall Water Splitting at Large Current Density. *Chem. Eng. J.* **2022**, *434*, 134669. [CrossRef]
18. Zhang, H.; Qian, G.; Chen, X.; Jiang, W.; Yu, T.; Wang, Y.; Luo, L.; Yin, S. V_2O_3-Decorated Spinel $CoFe_2O_4$ with Carbon-Encapsulated Mesoporous Nanosheets for Efficient Water Splitting. *ACS Sustain. Chem. Eng.* **2021**, *9*, 980–986. [CrossRef]
19. Wang, X.; Zhong, H.; Xi, S.; Lee, W.S.V.; Xue, J. Understanding of Oxygen Redox in the Oxygen Evolution Reaction. *Adv. Mater.* **2022**, *34*, 2107956. [CrossRef] [PubMed]
20. Wang, M.; Liu, D.; Srinivas, K.; Yu, H.; Ma, F.; Zhang, Z.; Wu, Y.; Li, X.; Wang, Y.; Chen, Y. $Ni_3S_4/FeNi_2S_4$ Heterostructure-Embedded Metal-Organic Framework-Derived Nanosheets Interconnected by Carbon Nanotubes for Boosting Oxygen Evolution Reaction. *Int. J. Hydrogen Energy* **2024**, *51*, 820–827. [CrossRef]
21. Xue, Q.; Wu, Y.; Hao, J.; Ma, L.; Dang, Y.; Zhu, J.-J.; Zhou, Y. NiO–$NiMoO_4$ Nanocomposites on Multi-Walled Carbon Nanotubes as Efficient Bifunctional Electrocatalysts for Total Water Splitting. *ACS Appl. Mater. Interfaces* **2023**, *15*, 31470–31477. [CrossRef] [PubMed]
22. Fan, M.; Dong, Q.; Ren, J.; Wang, H.; Wang, X.; Wang, R. In-Situ Self-Catalytically Grown CoNi-Doped C-N/CNT as a Binder-Free Electrocatalyst for High-Performance Oxygen Evolution Reaction. *J. Alloys Compd.* **2023**, *969*, 172289. [CrossRef]
23. Deng, X.; Mi, Y.; Liu, Y.; Sun, Y.; Cheng, Y.; Wang, W. Co, N Co-Doped Carbon Nanosheets Coupled with $NiCo_2O_4$ as an Efficient Bifunctional Oxygen Catalyst for Zn-Air Batteries. *Int. J. Hydrogen Energy* **2023**, *48*, 13452–13459. [CrossRef]
24. Liang, Y.; Li, Y.; Wang, H.; Zhou, J.; Wang, J.; Regier, T.; Dai, H. Co_3O_4 Nanocrystals on Graphene as a Synergistic Catalyst for Oxygen Reduction Reaction. *Nat. Mater.* **2011**, *10*, 780–786. [CrossRef] [PubMed]
25. Helal, M.H.; Thabet, H.K.; Aman, S.; Ahmad, N.; Tahir Farid, H.M.; El-Bahy, Z.M. One-Pot Formation of an RGO-Based $ZnAl_2O_4$ Nanocomposite for Electrochemical Studies toward Oxygen Evolution Reactions. *Energy Fuels* **2024**, *38*, 2273–2283. [CrossRef]
26. Mondal, S.; Mohanty, B.; Nurhuda, M.; Dalapati, S.; Jana, R.; Addicoat, M.; Datta, A.; Jena, B.K.; Bhaumik, A. A Thiadiazole-Based Covalent Organic Framework: A Metal-Free Electrocatalyst toward Oxygen Evolution Reaction. *ACS Catal.* **2020**, *10*, 5623–5630. [CrossRef]
27. Ghosh, A.; Mondal, M.; Nath Manna, R.; Bhaumik, A. Targeted Synthesis of a Metal-Free Thiadiazolate Based Nitrogen and Sulfur Rich Porous Organic Polymer for an Unprecedented Hydrogen Evolution in the Electrochemical Water Splitting. *J. Colloid. Interface Sci.* **2024**, *658*, 415–424. [CrossRef]
28. Huang, M.; Sun, C.; Zhang, X.; Wang, P.; Xu, S.; Shi, X. The Surface Structure, Stability, and Catalytic Performances toward O_2 Reduction of CoP and $FeCoP_2$. *Dalton Trans.* **2022**, *51*, 10420–10431. [CrossRef]
29. Zhang, W.; Xu, C.-H.; Zheng, H.; Li, R.; Zhou, K. Oxygen-Rich Cobalt–Nitrogen–Carbon Porous Nanosheets for Bifunctional Oxygen Electrocatalysis. *Adv. Funct. Mater.* **2022**, *32*, 2200763. [CrossRef]
30. Zhang, X.; Shao, J.; Huang, W.; Dong, X. Three Dimensional Carbon Substrate Materials for Electrolysis of Water. *Sci. China Mater.* **2018**, *61*, 1143–1153. [CrossRef]
31. Liu, X.; Zhang, Y.; Wang, W.; Chen, Y.; Xiao, W.; Liu, T.; Zhong, Z.; Luo, Z.; Ding, Z.; Zhang, Z. Transition Metal and N Doping on AlP Monolayers for Bifunctional Oxygen Electrocatalysts: Density Functional Theory Study Assisted by Machine Learning Description. *ACS Appl. Mater. Interfaces* **2022**, *14*, 1249–1259. [CrossRef]
32. Moon, J.; Beker, W.; Siek, M.; Kim, J.; Lee, H.S.; Hyeon, T.; Grzybowski, B.A. Active Learning Guides Discovery of a Champion Four-Metal Perovskite Oxide for Oxygen Evolution Electrocatalysis. *Nat. Mater.* **2024**, *23*, 108–115. [CrossRef]
33. Sun, C.; Duan, Z.; Wang, P.; Zhang, X.; Huang, M.; Cao, F.; Lin, W.; Wang, H.; Chen, Y.; Shi, X.-R. Modulation of Graphene and Graphdiyne by $Metal_n$ (n = 1–5) Adsorption and Nucleation and the Effect on Hydrogen Evolution Reaction. *Appl. Surf. Sci.* **2022**, *580*, 152197. [CrossRef]
34. Ma, C.; Feng, J.; Xia, C.; Du, C.; Chen, X.; Pang, B.; Dong, H.; Yu, L.; Dong, L. Theoretical Insights into Multi-Metal Atoms Embedded Nitrogen-Doped Graphene as Efficient Bifunctional Catalysts for Oxygen Reduction and Evolution Reactions. *Appl. Surf. Sci.* **2022**, *605*, 154714. [CrossRef]
35. Liu, X.; Li, G.; Liu, J.; Zhao, J. Transition Metal Atoms Anchored on Square Graphyne as Multifunctional Electrocatalysts: A Computational Investigation. *Mol. Catal.* **2022**, *531*, 112706. [CrossRef]
36. Wu, L.; Guo, T.; Li, T. Data-Driven High-Throughput Rational Design of Double-Atom Catalysts for Oxygen Evolution and Reduction. *Adv. Funct. Mater.* **2022**, *32*, 2203439. [CrossRef]
37. Fang, Z.; Li, S.; Zhang, Y.; Wang, Y.; Meng, K.; Huang, C.; Sun, S. The DFT and Machine Learning Method Accelerated the Discovery of DMSCs with High ORR and OER Catalytic Activities. *J. Phys. Chem. Lett.* **2024**, *15*, 281–289. [CrossRef]
38. Yao, W.; Qu, Y.; Zhou, M.; Wang, W.; Zhang, A.; Feng, Z.; Yan, H. Increasing the Bifunctional OER/ORR Activity of 3d Transition Metals Doped g-C_3N_3 by Controlling the Charge States. *Mol. Catal.* **2024**, *554*, 113807. [CrossRef]
39. Ye, Q.; Yi, X.; Wang, C.-Z.; Zhang, T.; Liu, Y.; Lin, S.; Fan, H.J. Data-Driven Screening of Pivotal Subunits in Edge-Anchored Single Atom Catalysts for Oxygen Reactions. *Adv. Funct. Mater.* **2024**, 2400107. [CrossRef]

40. Zhang, X.; Sun, C.; Xu, S.; Huang, M.; Wen, Y.; Shi, X.-R. DFT-Assisted Rational Design of CoMxP/CC (M = Fe, Mn, and Ni) as Efficient Electrocatalyst for Wide PH Range Hydrogen Evolution and Oxygen Evolution. *Nano Res.* **2022**, *15*, 8897–8907. [CrossRef]
41. Jia, Y.; Zhang, L.; Du, A.; Gao, G.; Chen, J.; Yan, X.; Brown, C.L.; Yao, X. Defect Graphene as a Trifunctional Catalyst for Electrochemical Reactions. *Adv. Mater.* **2016**, *28*, 9532–9538. [CrossRef]
42. Zhang, J.; Sun, Y.; Zhu, J.; Gao, Z.; Li, S.; Mu, S.; Huang, Y. Ultranarrow Graphene Nanoribbons toward Oxygen Reduction and Evolution Reactions. *Adv. Sci.* **2018**, *5*, 1801375. [CrossRef]
43. Li, D.; Zhang, A.; Feng, Z.; Wang, W. Theoretical Insights on the Charge State and Bifunctional OER/ORR Electrocatalyst Activity in 4d-Transition-Metal-Doped g-C_3N_4 Monolayers. *ACS Appl. Mater. Interfaces* **2024**, *16*, 5779–5791. [CrossRef]
44. Wang, P.; Shi, X.-R.; Zhang, Y.; Wei, M. The Influence of Co Nucleation in CoNi Single Atom Alloy on Low-Temperature Methane Dry Reforming with DFT Simulations and Microkinetic Modeling. *Mol. Catal.* **2023**, *549*, 113515. [CrossRef]
45. Cao, F.; Shi, X.R.; Wang, P.; Zhao, W.; Huang, M.; Hu, J.; Xu, S.; Zhao, G. Multistage Interface Engineered Cobalt Polysulfides Core-Shell Nanostructures for Dual Energy Storage Devices and Hydrogen Evolution. *Vacuum* **2023**, *216*, 112461. [CrossRef]
46. Li, H.; Jin, Z.; Lu, N.; Pan, J.; Xu, J.; Yin, X.-B.; Zhang, M. Fe_3O_4 Nanoparticles Entrapped in the Inner Surfaces of N-Doped Carbon Microtubes with Enhanced Biomimetic Activity. *Dalton Trans.* **2024**, *53*, 6974–6982. [CrossRef]
47. Li, Z.; Guo, Y.; Li, K.; Wang, S.; De Bonis, E.; Cao, H.; Mertens, S.F.L.; Teng, C. Shape Control of Bimetallic MOF/Graphene Composites for Efficient Oxygen Evolution Reaction. *J. Electroanal. Chem.* **2023**, *930*, 117144. [CrossRef]
48. Fan, F.; Huang, Q.; Rani, K.K.; Peng, X.; Liu, X.; Wang, L.; Yang, Z.; Huang, D.; Devasenathipathy, R.; Chen, D.-H.; et al. Interface and Doping Engineering of Co-Based Electrocatalysts for Enhanced Oxygen Reduction and Evolution Reactions. *Chem. Eng. J.* **2023**, *470*, 144380. [CrossRef]
49. Xiao, Y.; Gong, W.; Zhao, M.; Zhang, M.; Lu, N. Surface-Engineered Prussian Blue Nanozymes as Artificial Receptors for Universal Pattern Recognition of Metal Ions and Proteins. *Sens. Actuators B Chem.* **2023**, *390*, 134006. [CrossRef]
50. Jin, Z.; Li, H.; Zhang, L.; Pan, J.; Xu, J.; Yin, X.-B.; Zhang, M. Interfacing Ag_2S Nanoparticles and MoS_2 Nanosheets on Polypyrrole Nanotubes with Enhanced Catalytic Performance. *Inorg. Chem.* **2024**, *63*, 4260–4268. [CrossRef]
51. Tu, Y.; Ren, P.; Deng, D.; Bao, X. Structural and Electronic Optimization of Graphene Encapsulating Binary Metal for Highly Efficient Water Oxidation. *Nano Energy* **2018**, *52*, 494–500. [CrossRef]
52. Jing, S.; Wang, D.; Yin, S.; Lu, J.; Shen, P.K.; Tsiakaras, P. P-Doped CNTs Encapsulated Nickel Hybrids with Flower-like Structure as Efficient Catalysts for Hydrogen Evolution Reaction. *Electrochim. Acta* **2019**, *298*, 142–149. [CrossRef]
53. Yan, H.; Xie, Y.; Wu, A.; Cai, Z.; Wang, L.; Tian, C.; Zhang, X.; Fu, H. Anion-Modulated HER and OER Activities of 3D Ni–V-Based Interstitial Compound Heterojunctions for High-Efficiency and Stable Overall Water Splitting. *Adv. Mater.* **2019**, *31*, 1901174. [CrossRef]
54. Deng, J.; Ren, P.; Deng, D.; Bao, X. Enhanced Electron Penetration through an Ultrathin Graphene Layer for Highly Efficient Catalysis of the Hydrogen Evolution Reaction. *Angew. Chem. Int. Ed.* **2015**, *54*, 2100–2104. [CrossRef]
55. Lu, J.; Yin, S.; Shen, P.K. Carbon-Encapsulated Electrocatalysts for the Hydrogen Evolution Reaction. *Electrochem. Energy Rev.* **2019**, *2*, 105–127. [CrossRef]
56. Wang, S.; Huo, W.; Feng, H.; Xie, Z.; Shang, J.K.; Formo, E.V.; Camargo, P.H.C.; Fang, F.; Jiang, J. Enhancing Oxygen Evolution Reaction Performance in Prussian Blue Analogues: Triple-Play of Metal Exsolution, Hollow Interiors, and Anionic Regulation. *Adv. Mater.* **2023**, *35*, 2304494. [CrossRef]
57. Jiang, M.; Fan, X.; Cao, S.; Wang, Z.; Yang, Z.; Zhang, W. Thermally Activated Carbon–Nitrogen Vacancies in Double-Shelled NiFe Prussian Blue Analogue Nanocages for Enhanced Electrocatalytic Oxygen Evolution. *J. Mater. Chem. A Mater.* **2021**, *9*, 12734–12745. [CrossRef]
58. Guo, X.; Yue, K.; Zheng, J.; Yu, Z.; Wang, Y.; Liu, Y.; Liu, T.; Luo, J.; Tao, X.; Nai, J. Formation of Prussian Blue Analog Coronal Nanomaterials and Their Conversion into Mn–Co-Mixed Selenide for Enhanced Electrocatalytic Oxygen Evolution. *Mater. Chem. Front.* **2023**, *7*, 3728–3737. [CrossRef]
59. Zhao, P.; Fu, S.; Cheng, L.; Jiao, Z.; Wu, M. Modulating Zeolitic Imidazolate Framework-67 and Its Derivatives as Advanced Oxygen Evolution Reaction Electrocatalysts. *Coord. Chem. Rev.* **2024**, *498*, 215452. [CrossRef]
60. Chen, D.; Ji, X.; Zhou, X.; Sun, Q.; Xu, S.; Mao, L.; Guo, Z.; Guan, J.; Li, T.-T.; Qian, J. MOF-on-MOF-Derived Hollow $FeNi_3$/N-Doped Carbon Nanorods for Efficient Oxygen Evolution. *Chem. Eng. J.* **2023**, *470*, 144418. [CrossRef]
61. Lima, M.A.; Raimundo, R.A.; Araújo, A.J.; João, F.D.A.; Loureiro, F.J.A.; Macedo, D.A.; Morales, M.A. Nickel-Copper-Carbon Based Electrocatalysts for Oxygen Evolution Reaction: Sol-Gel Synthesis Using Chitosan. *Int. J. Hydrogen Energy* **2024**, *51*, 663–675. [CrossRef]
62. Nasri, A.; Jaleh, B.; Khazalpour, S.; Nasrollahzadeh, M.; Shokouhimehr, M. Facile Synthesis of Graphitic Carbon Nitride/Chitosan/Au Nanocomposite: A Catalyst for Electrochemical Hydrogen Evolution. *Int. J. Biol. Macromol.* **2020**, *164*, 3012–3024. [CrossRef]
63. Kayan, D.B.; İlhan, M.; Koçak, D. Chitosan-Based Hybrid Nanocomposite on Aluminium for Hydrogen Production from Water. *Ionics* **2018**, *24*, 563–569. [CrossRef]
64. Ding, J.; Zhong, L.; Huang, Q.; Guo, Y.; Miao, T.; Hu, Y.; Qian, J.; Huang, S. Chitosan Hydrogel Derived Carbon Foam with Typical Transition-Metal Catalysts for Efficient Water Splitting. *Carbon* **2021**, *177*, 160–170. [CrossRef]

65. Lei, Y.; Jia, M.; Guo, P.; Liu, J.; Zhai, J. MoP Nanoparticles Encapsulated in P-Doped Carbon as an Efficient Electrocatalyst for the Hydrogen Evolution Reaction. *Catal. Commun.* **2020**, *140*, 106000. [CrossRef]
66. Pu, Z.; Zhao, J.; Amiinu, I.S.; Li, W.; Wang, M.; He, D.; Mu, S. A Universal Synthesis Strategy for P-Rich Noble Metal Diphosphide-Based Electrocatalysts for the Hydrogen Evolution Reaction. *Energy Environ. Sci.* **2019**, *12*, 952–957. [CrossRef]
67. Ai, L.; Wang, Y.; Luo, Y.; Tian, Y.; Yang, S.; Chen, M.; Jiang, J. Robust Interfacial Ru-RuO_2 Heterostructures for Highly Efficient and Ultrastable Oxygen Evolution Reaction and Overall Water Splitting in Acidic Media. *J. Alloys Compd.* **2022**, *902*, 163787. [CrossRef]
68. Zhao, Y.; Lu, X.F.; Wu, Z.; Pei, Z.; Luan, D.; Lou, X.W. (David) Supporting Trimetallic Metal-Organic Frameworks on S/N-Doped Carbon Macroporous Fibers for Highly Efficient Electrocatalytic Oxygen Evolution. *Adv. Mater.* **2023**, *35*, 2207888. [CrossRef]
69. Yan, H.; Jiang, Z.; Deng, B.; Wang, Y.; Jiang, Z. Ultrathin Carbon Coating and Defect Engineering Promote RuO_2 as an Efficient Catalyst for Acidic Oxygen Evolution Reaction with Super-High Durability. *Adv. Energy Mater.* **2023**, *13*, 2300152. [CrossRef]
70. Sadhukhan, A.; Karmakar, A.; Koner, K.; Karak, S.; Sharma, R.K.; Roy, A.; Sen, P.; Dey, K.K.; Mahalingam, V.; Pathak, B.; et al. Functionality Modulation Toward Thianthrene-Based Metal-Free Electrocatalysts for Water Splitting. *Adv. Mater.* **2024**, *36*, 2310938. [CrossRef]
71. Karak, S.; Koner, K.; Karmakar, A.; Mohata, S.; Nishiyama, Y.; Duong, N.T.; Thomas, N.; Ajithkumar, T.G.; Hossain, M.S.; Bandyopadhyay, S.; et al. Morphology Tuning via Linker Modulation: Metal-Free Covalent Organic Nanostructures with Exceptional Chemical Stability for Electrocatalytic Water Splitting. *Adv. Mater.* **2024**, *36*, 2209919. [CrossRef] [PubMed]
72. Khan, I.; Baig, N.; Bake, A.; Haroon, M.; Ashraf, M.; Al-Saadi, A.; Tahir, M.N.; Wooh, S. Robust Electrocatalysts Decorated Three-Dimensional Laser-Induced Graphene for Selective Alkaline OER and HER. *Carbon* **2023**, *213*, 118292. [CrossRef]
73. Sekhon, S.S.; Lee, J.; Park, J.-S. Biomass-Derived Bifunctional Electrocatalysts for Oxygen Reduction and Evolution Reaction: A Review. *J. Energy Chem.* **2022**, *65*, 149–172. [CrossRef]
74. Zhao, Y.; Nakamura, R.; Kamiya, K.; Nakanishi, S.; Hashimoto, K. Nitrogen-Doped Carbon Nanomaterials as Non-Metal Electrocatalysts for Water Oxidation. *Nat. Commun.* **2013**, *4*, 2390. [CrossRef] [PubMed]
75. Murugan, N.; Thangarasu, S.; Seo, S.B.; Mariappan, A.; Choi, Y.R.; Oh, T.H.; Kim, Y.A. N-Doped Defect-Rich Porous Carbon Nanosheets Framework from Renewable Biomass as Efficient Metal-Free Bifunctional Electrocatalysts for HER and OER Application. *Renew. Energy* **2024**, *222*, 119801. [CrossRef]
76. Liu, Z.; Zhou, Q.; Zhao, B.; Li, S.; Xiong, Y.; Xu, W. Few-Layer N-Doped Porous Carbon Nanosheets Derived from Corn Stalks as a Bifunctional Electrocatalyst for Overall Water Splitting. *Fuel* **2020**, *280*, 118567. [CrossRef]
77. Li, M.; Liu, Z.; Wang, F.; Xuan, J. The Influence of the Type of N Dopping on the Performance of Bifunctional N-Doped Ordered Mesoporous Carbon Electrocatalysts in Oxygen Reduction and Evolution Reaction. *J. Energy Chem.* **2017**, *26*, 422–427. [CrossRef]
78. Huang, Y.; Wu, D.; Cao, D.; Cheng, D. Facile Preparation of Biomass-Derived Bifunctional Electrocatalysts for Oxygen Reduction and Evolution Reactions. *Int. J. Hydrogen Energy* **2018**, *43*, 8611–8622. [CrossRef]
79. Peng, X.; Zhang, L.; Chen, Z.; Zhong, L.; Zhao, D.; Chi, X.; Zhao, X.; Li, L.; Lu, X.; Leng, K.; et al. Hierarchically Porous Carbon Plates Derived from Wood as Bifunctional ORR/OER Electrodes. *Adv. Mater.* **2019**, *31*, 1900341. [CrossRef] [PubMed]
80. Pandey, K.; Jeong, H.K. Coffee Waste-Derived Porous Carbon for Hydrogen and Oxygen Evolution Reaction. *Chem. Phys. Impact* **2023**, *6*, 100175. [CrossRef]
81. Torres-Pinto, A.; Díez, A.M.; Silva, C.G.; Faria, J.L.; Sanromán, M.Á.; Silva, A.M.T.; Pazos, M. Tuning Graphitic Carbon Nitride (g-C_3N_4) Electrocatalysts for Efficient Oxygen Evolution Reaction (OER). *Fuel* **2024**, *360*, 130575. [CrossRef]
82. Zhang, H.; Yang, T.; Zhou, H.; Wang, Y.; Yang, X.; Liang, W.; Wu, D.; Yuan, P.; Yu, T.; He, M.; et al. Activating Fe Activity and Improving Ni Activity via C_3N_4 Substrate in Alkaline Oxygen Evolution Catalyzed by Ni-Fe Phosphide. *Appl. Catal. B* **2024**, *342*, 123391. [CrossRef]
83. Chen, M.; Zhang, Y.; Wang, R.; Zhang, B.; Song, B.; Guan, Y.; Li, S.; Xu, P. Surface Reconstruction of Se-Doped NiS_2 Enables High-Efficiency Oxygen Evolution Reaction. *J. Energy Chem.* **2023**, *84*, 173–180. [CrossRef]
84. Kang, T.; Kim, K.; Kim, M.; Kim, J. Electronic Structure Modulation of Nickel Hydroxide and Tungsten Nanoparticles for Fast Structure Transformation and Enhanced Oxygen Evolution Reaction Activity. *Chem. Eng. J.* **2021**, *418*, 129403. [CrossRef]
85. Chen, T.; Li, B.; Song, K.; Wang, C.; Ding, J.; Liu, E.; Chen, B.; He, F. Defect-Activated Surface Reconstruction: Mechanism for Triggering the Oxygen Evolution Reaction Activity of NiFe Phosphide. *J. Mater. Chem. A Mater.* **2022**, *10*, 22750–22759. [CrossRef]
86. Islam, M.; Tran, D.T.; Nguyen, T.H.; Dinh, V.A.; Kim, N.H.; Lee, J.H. Efficient Synergism of NiO-$NiSe_2$ Nanosheet-Based Heterostructures Shelled Titanium Nitride Array for Robust Overall Water Splitting. *J. Colloid. Interface Sci.* **2022**, *612*, 121–131. [CrossRef]
87. Wang, B.; Liu, Q.; Yuan, A.; Shi, Q.; Jiang, L.; Yang, W.; Yang, T.; Hou, X. A Facile and Green Strategy for Mass Production of Dispersive FeCo-Rich Phosphides@N,P-Doped Carbon Electrocatalysts toward Efficient and Stable Rechargeable Zn-Air Battery and Water Splitting. *J. Mater. Sci. Technol.* **2024**, *182*, 1–11. [CrossRef]
88. Wang, Y.-N.; Yang, Z.-J.; Yang, D.-H.; Zhao, L.; Shi, X.-R.; Yang, G.; Han, B.-H. $FeCoP_2$ Nanoparticles Embedded in N and P Co-Doped Hierarchically Porous Carbon for Efficient Electrocatalytic Water Splitting. *ACS Appl. Mater. Interfaces* **2021**, *13*, 8832–8843. [CrossRef]
89. Qin, Y.; Chai, R.; Tan, Z.; Hou, X.; Li, J.; Wu, F. A Ni-Fe-V Trimetallic Phosphorus-Selenium Composite Supported on Carbon Cloth as Freestanding Electrocatalyst for Oxygen Evolution Reaction. *Fuel* **2024**, *357*, 129857. [CrossRef]

90. He, X.; Qiao, T.; Zhang, Z.; Liu, H.; Wang, S.; Wang, X. Carbon Cloth Supporting Spinel $CuMn_{0.5}Co_2O_4$ Nanoneedles with the Regulated Electronic Structure by Multiple Metal Elements as Catalysts for Efficient Oxygen Evolution Reaction. *J. Colloid. Interface Sci.* **2023**, *649*, 635–645. [CrossRef]
91. Pan, F.; Huang, K.; Liu, P.; Li, R.; Lian, C.; Liu, H.; Hu, J. In Situ Electroactivated Fe-NiOOH Nanoclusters on Carbon Quantum Dots for Efficient Large-Scale Oxygen Production. *Small Struct.* **2022**, *3*, 2200094. [CrossRef]
92. Mehtab, A.; Ahmad, T. Unveiling the Bifunctional Photo/Electrocatalytic Activity of In Situ Grown CdSe QDs on g-C_3N_4 Nanosheet Z-Scheme Heterostructures for Efficient Hydrogen Generation. *ACS Catal.* **2024**, *14*, 691–702. [CrossRef]
93. Wu, X.; Li, S.; Wang, B.; Liu, J.; Yu, M. From Biomass Chitin to Mesoporous Nanosheets Assembled Loofa Sponge-like N-Doped Carbon/g-C_3N_4 3D Network Architectures as Ultralow-Cost Bifunctional Oxygen Catalysts. *Microporous Mesoporous Mater.* **2017**, *240*, 216–226. [CrossRef]
94. Mohana, P.; Swathi, S.; Yuvakkumar, R.; Ravi, G.; Thambidurai, M.; Nguyen, H.D. Co_3O_4/g-C_3N_4 Nanocomposite for Enriched Electrochemical Water Splitting. *Int. J. Hydrogen Energy* **2024**, *49*, 376–389. [CrossRef]
95. Vignesh, S.; Nam, S.; Kim, H. Interfacial Engineering of α-Fe_2O_3 Coupled Co_3O_4 Heterostructures Anchored on g-C_3N_4 Structure for Enhanced Electrocatalytic Performance in Alkaline Oxygen Evolution Reaction. *Int. J. Hydrogen Energy* **2024**, *53*, 1445–1456. [CrossRef]
96. Ricciardi, B.; da Silva Freitas, W.; Mecheri, B.; Nisa, K.U.; Montero, J.; Ficca, V.C.A.; Placidi, E.; Alegre, C.; D'Epifanio, A. Hierarchical Porous Fe/Ni-Based Bifunctional Oxygen Electrocatalysts for Rechargeable Zinc-Air Batteries. *Carbon* **2024**, *219*, 118781. [CrossRef]
97. Wen, Y.; Xu, S.; Wang, P.; Shao, X.; Sun, X.; Hu, J.; Shi, X.-R. Bimetallic FeCo Phosphide Nanoparticles Anchored on N-Doped Carbon Foam for Wide PH Hydrogen Evolution Reaction. *J. Alloys Compd.* **2023**, *931*, 167570. [CrossRef]
98. Liu, R.; Shi, X.-R.; Wen, Y.; Shao, X.; Su, C.; Hu, J.; Xu, S. Trimetallic Synergistic Optimization of 0D NiCoFe-P QDs Anchoring on 2D Porous Carbon for Efficient Electrocatalysis and High-Energy Supercapacitor. *J. Energy Chem.* **2022**, *74*, 149–158. [CrossRef]
99. Zhang, X.; Shi, X.-R.; Wang, P.; Bao, Z.; Huang, M.; Xu, Y.; Xu, S. Bio-Inspired Design of NiFeP Nanoparticles Embedded in (N,P) Co-Doped Carbon for Boosting Overall Water Splitting. *Dalton Trans.* **2023**, *52*, 6860–6869. [CrossRef]
100. Yang, Y.; Zhu, B.; Guo, P.-F.; Wang, W.-J.; Wang, W.-T.; Wang, K.; He, Z.-H.; Liu, Z.-T. Core-Shell Trimetallic NiFeV Disulfides and Amorphous High-Valance NiFe Hydroxide Nanosheets Enhancing Oxygen Evolution Reaction. *Chem. Eng. J.* **2022**, *430*, 133047. [CrossRef]
101. Chen, F.; Shen, C.; Zhu, Y.; Liu, Y.; Zhou, D.; Huang, L.; Shi, L.; Zhang, H.; Cao, S.; Jia, R. Magnetic Field Enhanced Surface Reconstruction of Fe_2P and the Promotional Effect in Electrochemical Oxygen Evolution. *Appl. Surf. Sci.* **2024**, *653*, 159357. [CrossRef]
102. Kim, T.; Kim, S.; Jeong, H.; Im, Y.; Park, N.; Kang, M. Improved OH Adsorption and Effective Oxygen Evolution Reaction on Carbon-Capsulated $Co_{0.1}Ni_{0.9}O$@C/CP Electrode. *Appl. Surf. Sci.* **2024**, *655*, 159549. [CrossRef]
103. Zhang, Y.; Wei, S.; Xing, P.; Dai, L.; Wang, Y. Iron-Doped Nickel Sulfide Nanoparticles Grown on N-Doped Reduced Graphene Oxide as Efficient Electrocatalysts for Oxygen Evolution Reaction. *J. Electroanal. Chem.* **2023**, *936*, 117323. [CrossRef]
104. Zhang, S.; Zhang, X.; Shi, X.; Zhou, F.; Wang, R.; Li, X. Facile Fabrication of Ultrafine Nickel-Iridium Alloy Nanoparticles/Graphene Hybrid with Enhanced Mass Activity and Stability for Overall Water Splitting. *J. Energy Chem.* **2020**, *49*, 166–173. [CrossRef]
105. Hu, Y.; Zhao, X.; Li, F.; Dong, Q.; Wen, B.; Sun, D.; Liang, W.; Lyu, X. Spherical $ZnFe_2O_4$ Nanoparticles on Nitrogen-Doped Graphene: A Synergistic Effect on Efficient Electrocatalytic Oxygen Evolution Reaction. *ACS Appl. Energy Mater.* **2023**, *6*, 9985–9993. [CrossRef]
106. Lin, Y.-C.; Aulia, S.; Yeh, M.-H.; Hsiao, L.-Y.; Tarigan, A.M.; Ho, K.-C. Graphene Quantum Dots Induced Defect-Rich NiFe Prussian Blue Analogue as an Efficient Electrocatalyst for Oxygen Evolution Reaction. *J. Colloid. Interface Sci.* **2023**, *648*, 193–202. [CrossRef] [PubMed]
107. Deng, S.; Zhang, X.; Zhang, Y.; Ye, J.; Mei, B.; Lin, S. Flower-like Iron Sulfide/Cobaltous Sulfide Heterostructure as Advanced Electrocatalyst for Oxygen Evolution Reaction. *Int. J. Hydrogen Energy* **2023**, *51*, 550–557. [CrossRef]
108. Wang, L.; Huang, J.; Huang, Z.; Li, H.; Taylor Isimjan, T.; Yang, X. Revealing Dynamic Structural Evolution of V and P Co-Doping-Induced Co Defects as Large-Current Water Oxidation Catalyst. *Chem. Eng. J.* **2023**, *472*, 144924. [CrossRef]
109. Gao, D.; Zhu, W.; Chen, J.; Qin, K.; Ma, M.; Shi, J.; Wang, Q.; Fan, Z.; Shao, Q.; Liao, F.; et al. High-Entropy Effect Promoting Self-Healing Behavior of Two-Dimensional Metal Oxide Electrocatalysts for Oxygen Evolution Reaction. *ACS Catal.* **2024**, *14*, 3700–3711. [CrossRef]
110. Shao, X.; Xu, S.; Wang, P.; Wen, Y.; Sun, X.; Hong, M.; Wu, K.; Shi, X.-R. Carbon-Incorporated Bimetallic Phosphide Nanospheres Derived from MOFs as Superior Electrocatalysts for Hydrogen Evolution. *Dalt Trans.* **2022**, *51*, 14517–14525. [CrossRef]
111. Zhao, Y.; Liu, J.; Zhang, T.; Liu, F.; Zheng, M.; Shi, K.; Liu, J.; Zhang, Y.; Wang, H. Synthesis of Novel Hollow Carbon Nanotubes @ Co-Fe Alloy/Iron Phthalocyanine Electrocatalyst by Self-Assembly Method for OER and ORR Study. *Colloids Surf. A Physicochem. Eng. Asp.* **2024**, *684*, 133093. [CrossRef]
112. An, Y.; Ren, Z.; Kong, Y.; Tian, Y.; Jiang, B.; Shaik, F. Fluorine-Based Multi-Halogen Atom Doped Vinasse Carbon Quantum Dots on Vertical Graphene: A Bifunctional Catalytic Electrode for Water Splitting. *Int. J. Hydrogen Energy* **2024**, *58*, 633–645. [CrossRef]
113. Zhang, R.; Lu, N.; Zhang, J.; Yan, R.; Li, J.; Wang, L.; Wang, N.; Lv, M.; Zhang, M. Ultrasensitive Aptamer-Based Protein Assays Based on One-Dimensional Core-Shell Nanozymes. *Biosens. Bioelectron.* **2020**, *150*, 111881. [CrossRef] [PubMed]

114. Zeng, C.; Lu, N.; Wen, Y.; Liu, G.; Zhang, R.; Zhang, J.; Wang, F.; Liu, X.; Li, Q.; Tang, Z.; et al. Engineering Nanozymes Using DNA for Catalytic Regulation. *ACS Appl. Mater. Interfaces* **2019**, *11*, 1790–1799. [CrossRef] [PubMed]
115. Wang, J.; Yin, H.; Chen, Z.; Cao, G.; Xu, N.; Wu, H.; Wang, P. A Core-Shell Structured $CoMoO_4 \cdot nH_2O$@$Co_{1-x}Fe_xOOH$ Nanocatalyst for Electrochemical Evolution of Oxygen. *Electrochim. Acta* **2020**, *345*, 136125. [CrossRef] [PubMed]
116. Li, M.; Tao, L.; Xiao, X.; Lv, X.; Jiang, X.; Wang, M.; Peng, Z.; Shen, Y. Core-Shell Structured $NiCo_2O_4$@FeOOH Nanowire Arrays as Bifunctional Electrocatalysts for Efficient Overall Water Splitting. *ChemCatChem* **2018**, *10*, 4119–4125. [CrossRef]
117. Wu, J.; Wang, Z.; Guan, T.; Zhang, G.; Zhang, J.; Han, J.; Guan, S.; Wang, N.; Wang, J.; Li, K. Optimizing Band Structure of CoP Nanoparticles via Rich-defect Carbon Shell toward Bifunctional Electrocatalysts for Overall Water Splitting. *Carbon. Energy* **2023**, *5*, e268. [CrossRef]
118. Nan, Y.; Liu, T.; Liu, W.; Cao, D.; Cheng, D. Constructing Chainmail-Structured CoP/C Nanospheres as Highly Active Anodic Electrocatalysts for Oxygen Evolution Reaction. *ACS Appl. Mater. Interfaces* **2024**, *16*, 16309–16316. [CrossRef] [PubMed]
119. Kong, D.; Xu, Q.; Chu, N.; Wang, H.; Lim, Y.V.; Cheng, J.; Huang, S.; Xu, T.; Li, X.; Wang, Y.; et al. Rational Construction of 3D Self-Supported MOF-Derived Cobalt Phosphide-Based Hollow Nanowall Arrays for Efficient Overall Water Splitting at Large Current Density. *Small* **2024**, 2310012. [CrossRef]
120. Lv, X.; Xu, W.; Tian, W.; Wang, H.; Yuan, Z. Activity Promotion of Core and Shell in Multifunctional Core–Shell Co_2P@NC Electrocatalyst by Secondary Metal Doping for Water Electrolysis and Zn-Air Batteries. *Small* **2021**, *17*, 2101856. [CrossRef]
121. Abbas, S.A.; Ma, A.; Seo, D.; Jung, H.; Lim, Y.J.; Mehmood, A.; Nam, K.M. Synthesis of Fe_3C@C Core-Shell Catalysts with Controlled Shell Composition for Robust Oxygen Evolution Reaction. *Appl. Surf. Sci.* **2021**, *551*, 149445. [CrossRef]
122. Wang, P.; Bai, P.; Mu, J.; Jing, J.; Wang, L.; Su, Y. N, S Codoped Carbon Matrix-Encapsulated CoFe/$Co_{0.2}Fe_{0.8}S$ Heterostructure as a Highly Efficient and Durable Bifunctional Oxygen Electrocatalyst for Rechargeable Zinc-Air Batteries. *J. Colloid. Interface Sci.* **2023**, *642*, 1–12. [CrossRef] [PubMed]
123. Alhakemy, A.Z.; Elseman, A.M.; Fayed, M.G.; Ahmed Amine Nassr, A.B.; El-Hady Kashyout, A.; Wen, Z. Hybrid Electrocatalyst of $CoFe_2O_4$ Decorating Carbon Spheres for Alkaline Oxygen Evolution Reaction. *Ceram. Int.* **2022**, *48*, 5442–5449. [CrossRef]
124. Zhao, J.; Niu, Q.; Zhang, J.; Zhang, P. Core–Shell Construction of Metal@carbon by Mechanochemically Recycling Plastic Wastes: Towards an Efficient Oxygen Evolution Reaction. *Green. Chem.* **2023**, *25*, 8047–8056. [CrossRef]
125. Gao, T.; Yu, S.; Chen, Y.; Li, X.; Tang, X.; Wu, S.; He, B.; Lan, H.; Li, S.; Yue, Q.; et al. Regulating the Thickness of the Carbon Coating Layer in Iron/Carbon Heterostructures to Enhance the Catalytic Performance for Oxygen Evolution Reaction. *J. Colloid. Interface Sci.* **2023**, *642*, 120–128. [CrossRef] [PubMed]
126. Wang, S.; Huo, W.; Fang, F.; Xie, Z.; Shang, J.K.; Jiang, J. High Entropy Alloy/C Nanoparticles Derived from Polymetallic MOF as Promising Electrocatalysts for Alkaline Oxygen Evolution Reaction. *Chem. Eng. J.* **2022**, *429*, 132410. [CrossRef]
127. Ma, L.; Wei, Z.; Zhao, C.; Meng, X.; Zhang, H.; Song, M.; Wang, Y.; Li, B.; Huang, X.; Xu, C.; et al. Hierarchical Superhydrophilic/Superaerophobic 3D Porous Trimetallic (Fe, Co, Ni) Spinel/Carbon/Nickel Foam for Boosting Oxygen Evolution Reaction. *Appl. Catal. B* **2023**, *332*, 122717. [CrossRef]
128. Wei, L.; Chen, Y. Degradation of Carbon Materials in Electrocatalysis. *Curr. Opin. Electrochem.* **2022**, *36*, 101159. [CrossRef]
129. Wang, C.; Zhai, P.; Xia, M.; Liu, W.; Gao, J.; Sun, L.; Hou, J. Identification of the Origin for Reconstructed Active Sites on Oxyhydroxide for Oxygen Evolution Reaction. *Adv. Mater.* **2023**, *35*, 2209307. [CrossRef]
130. Righi, G.; Plescher, J.; Schmidt, F.-P.; Campen, R.K.; Fabris, S.; Knop-Gericke, A.; Schlögl, R.; Jones, T.E.; Teschner, D.; Piccinin, S. On the Origin of Multihole Oxygen Evolution in Haematite Photoanodes. *Nat. Catal.* **2022**, *5*, 888–899. [CrossRef]
131. Haase, F.T.; Bergmann, A.; Jones, T.E.; Timoshenko, J.; Herzog, A.; Jeon, H.S.; Rettenmaier, C.; Cuenya, B.R. Size Effects and Active State Formation of Cobalt Oxide Nanoparticles during the Oxygen Evolution Reaction. *Nat. Energy* **2022**, *7*, 765–773. [CrossRef]

Disclaimer/Publisher's Note: The statements, opinions and data contained in all publications are solely those of the individual author(s) and contributor(s) and not of MDPI and/or the editor(s). MDPI and/or the editor(s) disclaim responsibility for any injury to people or property resulting from any ideas, methods, instructions or products referred to in the content.